ABSTRACT

Title of dissertation: OPTICAL AND THERMAL PROPERTIES OF NANOPOROUS MATERIAL AND DEVICES

Kyowon Kim, Doctor of Philosophy, 2015

Dissertation directed by: Professor Thomas E. Murphy
Dept. of Electrical & Computer Engineering

In this thesis, we investigate the optical and thermal properties of porous silicon and its applications. In first part, porous silicon's optical properties and application as a highly sensitive refractive index sensor is studied. An integrated Mach-Zehnder interferometer waveguide fabricated from nanoporous silicon is shown to exhibit high sensitivity and measurement stability that exceeds previously demonstrated porous sensors. In second part, we discuss experimental methods to characterize the thermal conductivity of nanoporous silicon films. We use the 3-ω method to characterize the exceptionally low thermal conductivity of porous silicon. Finally, we employ an improved heat conduction analysis method for the 3-ω method to measure the anisotropy in thermal conductivity. Our measurement show that porous silicon has very low in-plane thermal conductivity compared to cross-plane conductivity. We confirmd this anisotropy using direct numerical simulation of the anisotropic heat equation.

OPTICAL AND THERMAL PROPERTIES OF NANOPOROUS MATERIAL AND DEVICES

by

Kyowon Kim

Dissertation submitted to the Faculty of the Graduate School of the
University of Maryland, College Park in partial fulfillment
of the requirements for the degree of
Doctor of Philosophy
2015

Advisory Committee:
Professor Thomas E. Murphy, Chair/Advisor
Professor Christopher C. Davis
Professor Yu Chen
Professor R. D. Gomez
Professor Oded Rabin

Acknowledgments

I would like to thank all people who have supported and encouraged me throughout my Ph.D. study.

Firstly, I would like to express my sincere gratitude to my advisor Prof. Thomas Murphy for the continuous support and guidence of my Ph.D study. I have learned a lot about how to find and approach a problem, the ways to resolve it and effectively presenting my work from him. He has always been supportive whenever I need help for either my work or personal difficulty. His guidance helped me in all the time of research and writing of this thesis. I could not have imagined having a better advisor and mentor for my Ph.D study.

Besides, I would like to thank the rest of my thesis committee: Prof. Christopher Davis, Prof. Yu Chen, Prof. R. D. Gomez and Prof. Oded Rabin for their insightful comments and encouragement, but also for the hard question which incented me to widen my research from various perspectives.

I greatly appreciate my fellow group members who helped and inspired me. Dr. Alen Lo, in spite of short period time we worked together, taught me a lot of experimental skills. What I have learn from him became a cornerstone of my early research. I have benefited from discussion with Ryan Suess during many parts of my research, especially experimantal design and instrumentation. I enjoyed working with Dr. Gagan Kumar and Shanshan Li on several fabrication projects. I also appreciate Mehdi Jadidi helping me on numerical simulation. Vincent Pagan and J.J. Wathen gave me helpful advices on fiber optic experimental techniques.

Also, discussion with Dr. Larry Hess and Dr. Ari Brown from NASA Goddard Space Flight Center was very helpful for thermal property investigation.

I would like to thank all of my friends whom I met in College Park. The life during my Ph.D. study would have been less enjoyable without them.

I am grateful to my wife, Nahyeon, for her love, support and encouragement. She has always been standing by me to help achieving my goal. Last but not the least, I would like to thank my parents who always pray for me and my family from overseas.

Table of Contents

List of Tables vi

List of Figures vii

List of Abbreviations x

1 Introduction 1
1.1 Porous waveguide sensor 1
1.2 Thermal conductivity 3

2 Integrated Mach-Zehnder interferometer waveguide sensor 6
2.1 Fabrication 10
2.1.1 Slab waveguide Fabrication 10
2.1.2 Channel waveguide 13
2.1.3 Planarization and window etching 15
2.2 Characterization 16
2.2.1 Single mode operation 16
2.2.2 Loss measurement 17
2.3 Experimental results 18
2.3.1 Stability comparison between integrated MZI and fiber optic MZI 21
2.3.2 Sensor performance measurement 22
2.3.3 Heterodyne phase shift measurement 23
2.3.4 Sensitivity analysis 24
2.4 Summary 26

3 Thermal conductivity of porous silicon 27
3.1 Prior thermal measurement of porous silicon 27
3.2 3-ω method 28
3.2.1 3ω voltage and temperature oscillation 29
3.2.2 Temperature oscillation of line heater on semi-infinite substrate 31
3.3 Differential 3-ω method 34

3.3.1 1-dimensional thermal resistor model . . . 35
3.3.2 Temperature difference measurement . . . 36
3.4 Instrumentation . . . 37
3.5 Sample fabrication and characterization . . . 40
3.5.1 Fabrication . . . 40
3.5.2 Resistance thermometry . . . 42
3.5.3 Porosity estimation . . . 43
3.6 Results and discussion . . . 44
3.6.1 Reference (SiO_2) sample . . . 44
3.6.2 Porous silicon from moderately doped substrate . . . 45
3.6.3 Porous silicon from highly doped substrate . . . 46
3.7 Summary . . . 48

4 Strong anisotropic thermal conductivity of porous silicon 49
4.1 2D heat flow model . . . 51
4.1.1 Multilayer film on substrate . . . 51
4.1.2 Single anisotropic film on isotropic substrate . . . 52
4.1.3 Sample Fabrication . . . 57
4.1.4 Experimental result and discussion . . . 58
4.2 Numerical simulation with comparable experiment . . . 68
4.2.1 Simulation . . . 68
4.2.2 Experiment . . . 70
4.2.3 Result and discussion . . . 70
4.3 Summary . . . 73

5 Conclusion 75
5.1 Summary . . . 75
5.2 Future work . . . 76
5.2.1 Thermo-optic modulator . . . 76
5.2.2 Non-contact method to investigate anisotropic thermal property 78

Bibliography 80

List of Tables

3.1 Previously reported thermal conductivity of porous silicon 28
3.2 $k_{PSi,z}$ measurement result for moderately doped porous silicon 46
3.3 $k_{PSi,z}$ measurement result for highly doped porous silicon 47

4.1 List of samples with different PSi thickness (d) and heater width ($2b$). 59
4.2 Sample dimensions and thermal conductivities ($k_{PSi,z}$) estimated by 1D assumption. 65

List of Figures

1.1 SEM micrograph of porous silicon. Left: top down view, Right: cross sectional view 2

2.1 Fabrication process used to produce integrated porous silicon waveguides. (a) A three-layer planar waveguide is formed by electrochemical etching of crystalline silicon. (b) Two parallel lines are inscribed using direct-write laser oxidation, to form the left and right boundaries of the optical waveguide. (c) The oxidized regions are removed in a solution of dilute HF. (d) A planarizing polymer layer (CYTOP) is spin-coated over the structure. (e) The sensing window is photolithographically defined, and (f) reactive ion etching is used to expose the underlying porous silicon waveguide. 8

2.2 Electrochemical etching system used to fabricate nanoporous silicon devices 11

2.3 (a) Optical reflectance measurement and (b) profilometry measurement used to measure the refractive index and electrochemical etch rate, respectively. 11

2.4 Refractive index vs. current density (left) and etch rate vs. current density (right) calibration result 12

2.5 (a) Schematic of integrated MZI waveguide. (b) Cross-sectional scanning electron micrograph (SEM) of a single waveguide. (c) Optical micrograph of Y-branch. (d) Optical micrograph showing selectively exposed sensing window in one arm of the interferometer. 13

2.6 Scanning laser oxidation system 14

2.7 SEM micrographs of cross sectional view of grooves fabricated by (a) 473 nm, (b) 532 nm and (c) 980 nm. 15

2.8 Experimental setup for observing optical modes from the output facet 17

2.9 Observations of optical pattern emerging from porous silicon waveguide for (a) singlemode waveguide with y-branch, (b) multimode optical waveguide with y-branch, (c) singlemode straight waveguide and (d) multimode straight waveguide. 18

2.10 Propagation loss estimation by cutback measurement 19

2.11 Experimental setups used to conduct interferometric porous waveguide measurements. (a) Integrated Mach-Zehnder interferometer (MZI) constructed using porous silicon waveguides. (b) Fiber-based MZI, with porous waveguide incorporated in one arm of interferometer, and (c) Heterodyne fiber-based interferometer, enabling simultaneous measurement of magnitude and phase shift in porous waveguide sensor. 20
2.12 Comparison of stability from integrated porous Mach-Zehnder interferometer and fiber-based waveguide interferometer, conducted over 400 s with no analyte present. Prior to observation, both systems were adjusted to have full interferometric fringe contrast and equal fringe amplitude. 22
2.13 Interference signal measured from (a) integrated nanoporous silicon MZI device and (b) straight waveguide incorporated into an external fiber MZI. The interference signal is observed over a 400 s time interval during which a drop of isopropanol is introduced to the porous waveguide. 23
2.14 Heterodyne measurement of intensity and phase change from a 200 μm porous silicon waveguide that is exposed to isopropanol. 24

3.1 (a) Simplified 3-ω measurement diagram. (b) Relationship between current, heat power, temperature, electrical resistance and voltage. . . 29
3.2 Line heater on semi-infinite substrate model 32
3.3 (a) Temperature gradient (heat flow) inside a typical 'thin film on substrate' sample for differential 3-ω measurement. (b) Ideal sample structure (micro-mesa) for differential 3-ω measurement. (c) Temperature oscillation of top and bottom interfaces of the film in time domain. (d) Amplitude of temperature oscillation of the two differential 3-ω measurement samples 35
3.4 Diagram of 3-ω thermal conductivity measurement setup 37
3.5 Schematic diagram of 3-ω measurement circuit with approximate current source 39
3.6 3-ω sample fabrication process. (a) Porous silicon layer is formed by electrochemical etching. (b) PECVD SiO_2 is deposited for electrical insulation. (c) Photoresist is spin-coated and patterned. (d) 200 nm Aluminum is deposition and excessive area is lifted-off. (e) Heater design (f) Completed sample 41
3.7 Electrical resistance of heater as a function of temperature 43
3.8 $\theta_{2\omega}/P$ as a function of $\ln 2\omega$, blue is bare intrinsic silicon and green is thermal SiO_2 on intrinsic silicon. 44
3.9 θ/P as a function of $\ln 2\omega$, blue is bare intrinsic silicon. Green and red are 1 μm and 2 μm of PSi on substrate. Top: porosity of 64.9 % Bottom: porosity of 61.4 % 45
3.10 θ/P as a function of $\ln 2\omega$, blue is bare intrinsic silicon. Green and red are 1 μm and 2 μm of PSi on substrate. 47

4.1 Multilayer film on substrate 2D heat flow model 52
4.2 Anisotropic film on substrate 53
4.3 $F(\beta_F)$ as a function of β_F 55
4.4 Prepared sample with highest b/d (left) and lowest b/d (right). 58
4.5 The heater resistance vs. temperature of samples with 6 different heater width 60
4.6 Results of reference samples (samples 1 - 6). Numbers in legend represent heater widths. 61
4.7 Samples 1, 7, 13, 25. Heaters' nominal width is 4 μm. '$d = 0$ μm' represents no-PSi sample (reference). 62
4.8 Samples 2, 8, 14, 19, 26. Heaters' nominal width is 10 μm. '$d = 0$ μm' represents no-PSi sample (reference). 62
4.9 Samples 3, 9, 15, 20, 27. Heaters' nominal width is 16 μm. '$d = 0$ μm' represents no-PSi sample (reference). 63
4.10 Samples 4, 10, 16, 21, 28. Heaters' nominal width is 22 μm. '$d = 0$ μm' represents no-PSi sample (reference). 63
4.11 Samples 5, 11, 17, 22, 29. Heaters' nominal width is 28 μm. '$d = 0$ μm' represents no-PSi sample (reference). 64
4.12 Samples 6, 12, 18, 23, 30. Heaters' nominal width is 34 μm. '$d = 0$ μm' represents no-PSi sample (reference). 64
4.13 Estimated thermal conductivity with 1D assumption as a function of "heater width/PSi thickness" ratio 66
4.14 Estimated $k_{PSi,z}$ with $k_{PSi,x} \approx 0$, $k_{PSi,x} = 0.45\ \mathrm{Wm^{-1}K^{-1}}$ and $k_{PSi,x} = k_{PSi,z}$ assumptions 67
4.15 Schematic diagram of the numerical simulation model 69
4.16 Comparison of heat spreading inside sample between isotropic and anisotropic case by numerical simulation. 71
4.17 Comparison between experimental data and numerical simulation. . . 72

List of Abbreviations and Symbols

α	Temperature coefficent of resistance
ω	Angular frequency
θ	Temperature difference
b	Heater half width
CTE	Coefficient of Thermal Expansion
D	Thermal diffusivity
d	Porous silicon / film thickness
I	Electrical current
k	Thermal conductivity
L	Heater length
MZI	Mach-Zehnder Interferometer
P	Electrical power
PSi	Porous Silicon
Q	Heat flow
R_e	Electrical resistance
R_t	Thermal resistance
SEM	Scanning Electron Microscope
T	Temperature
T_0	Environmental temperature
V	voltage
x	Axis of in-plane direction
z	Axis of cross-plane direction

Chapter 1: Introduction

Porous silicon, since initial demonstration of room temperature photoluminescence in 1990 [1], been attracting attention because of its unique optical, electrical and thermal properties compared to crystalline silicon. It is an interesting material comprised of nanoscale pores in crystalline silicon, which is typically formed by electrochemical etching in hydrofluoric acid electrolyte. Its porosity and pore size depends on etching current density and doping concentration of substrate silicon wafer. It exhibits many physical properties that are quite different from its crystalline counterpart, including linear & nonlinear optical properties, electrical properties, thermal properties and anisotropy.

1.1 Porous waveguide sensor

Like crystalline silicon from which it is formed, porous silicon can be used as an optical material that is transparent at infrared wavelengths. Because the pore size is smaller than the optical wavelength, it behaves as an effective dielectric with optical properties between those of silicon and air or material inside of the pores. Porous silicon is also a favorable optical material in terms of fabrication. Because the porosity can be easily controlled by the etching process, it is easy to achieve

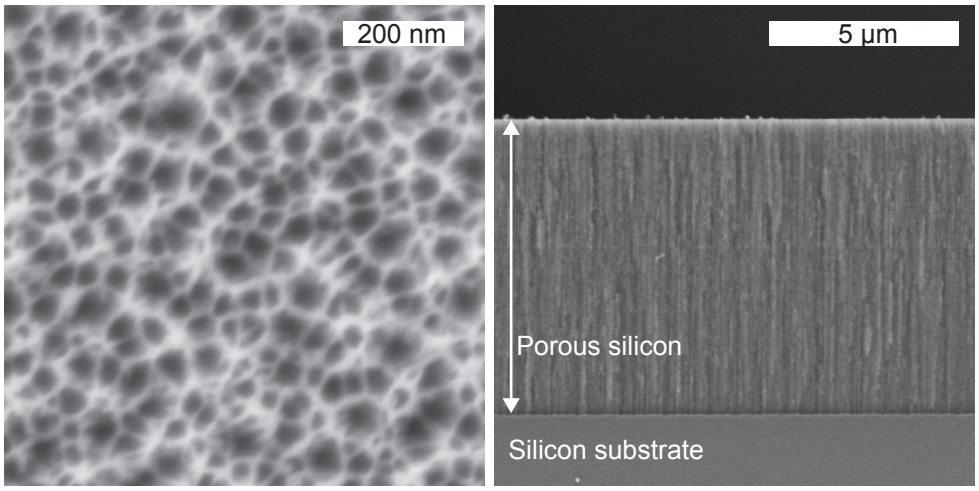

Figure 1.1: SEM micrograph of porous silicon. Left: top down view, Right: cross sectional view

single layer with desired refractive index or multiple layers with different index, which is great advantage for fabricating waveguides or multilayer optical structures such as Bragg reflectors or resonant cavities [2, 3].

Porous silicon is a excellent platform for chemical or biological sensor. Its extremely high surface area to volume ratio (over 500 cm^{-1}) enables concentrating nano scale substance in small volume, therefore makes it easier to be detected. The pore surface can be functionalized to selectively bind a substance to be detected such as DNA, proteins and viruses [4, 5]. Combined with previously mentioned optical properties, porous silicon is able to serve as an optical sensor material. Several porous silicon sensor designs have been proposed and demonstrated. Many prior devices rely on observation of the reflection interference spectrum from porous structures, including single layers [6, 7], Bragg mirrors [8, 9] or resonant cavities [10–14]. Transmission measurements have also been achieved by measuring the change in

birefringence when a free-standing porous substrate is filled with a solvent or analyte [15, 16]. All of these devices that utilize an optical path that is perpendicular to porous silicon substrate, and therefore inherently suffer from limited sensitivity because of the short interaction length. Furthermore, many of them require a relatively wide-range tunable laser or broadband light source to detect shifts in the spectral interference pattern.

A solution to this issue is to employ a waveguide structure that confines light in two dimensions and guides parallel to substrate. This design allows for relatively long interaction length by simply extending the length of sensing area. We proposed and successfully demonstrated this device with improved sensitivity compared to previous studies. [17]

1.2 Thermal conductivity

Porous silicon also exhibits thermal properties that are different from crystalline silicon. While crystalline silicon is a good thermal conductor (150 $\mathrm{Wm^{-1}K^{-1}}$) [18, 19], thermal conductivity of porous silicon is much lower than crystalline silicon and also tunable by controlling the porosity. Studies have been conducted to measure the thermal conductivity of porous silicon using several different methods including electrical AC heating (3-ω method)Gesele1997, photo-acoustic [20,21], micro-Raman [22–24] and scanning thermal microscopy [25]. Prior studies show that thermal conductivity of porous silicon can be as low as 0.2 $\mathrm{Wm^{-1}K^{-1}}$ [26] which is 3 orders of magnitude smaller than bulk silicon. We used the 3-ω method [27–29]

to measure thermal conductivity of porous silicon of several different parameters and confirmed that the values are comparable to previous studies. Because it exhibits such a low thermal conductivity, porous silicon could be used for applications that require thermal isolation, including bolometer, micro heater and thermo optic modulators. The ability being able to build an insulation structure with same material as silicon substrate is especially important for devices that must operate in extremely high or low temperature environment. Traditional thermal insulation materials that have a coefficient of thermal expansion (CTE) different form that of silicon can cause layers to be peel or de-laminate when the device is cooled or heated because of the different expansion ratio. Porous silicon is advantageous in this aspect because it is not only same material but also maintains the same crystalline structure as the substrate, therefore almost eliminates possibility such mechanical stress failure related to the CTE mismatch.

One application that specifically requires control and engineering of the thermal isolation is in infrared bolometers [30,31]. The detection speed and sensitivity of bolometer are critically dependent on the device's thermal design. Because they are often operated in cooled environment, having insulation material with same CTE as substrate is also important. The most sensitive bolometers often employ suspended thin film design for thermal isolation, therefore in-plane directional thermal conductivity of material is an important factor. Also, crosstalk between adjacent pixels in microbolometer arrays is limited by in-plane conduction. Porous silicon is expected to be thermally anisotropic because, unlike isotropic materials, porous silicon has directional, columnar microscopic structure (c.f. Fig. 1.1 (b)). To date,

the in-plane thermal conductivity of porous silicon has not been studied. In-plane thermal conductivity can ideally be measured with suspended thin film, however it is very challenging to fabricate suspended thin porous silicon film. We describe in Chapter 4, a variable line-width 3-ω measurement that measures in-plane component indirectly.

Chapter 2: Integrated Mach-Zehnder interferometer waveguide sensor

Optical sensors are attracting attention for a variety of applications including medical diagnostics, environmental monitoring, security and manufacturing. The ability to remotely probe, sense, diagnose or measure a target analyte through optical means is particularly important in applications that are otherwise not amenable to or accessible by electrical means. Waveguide-based optical sensing systems are more appealing than those based on bulk measurements because they offer the possibility for miniaturization, integration and parallelization.

Many optical waveguide sensors rely on a small refractive index change that occurs when a target analyte binds to or otherwise interacts with an optical surface. One of the most studied refractive index sensor designs is the solid core evanescent wave sensor, which relies on the small overlap between the evanescent tail of an optical mode with a surface-bound analyte [32–35] – typically a weak effect that requires a long interaction length to produce a measurable signal. Moreover, exposing the evanescent tail of the mode can make an optical waveguide susceptible to macroscopic particles and other unwanted contaminants (in addition to the analyte) that impair the function of the sensor. More recently, microfluidic waveguide sensors

have been introduced to overcome limitations of evanescent wave sensors [36, 37], however the need for microfluidic circulation can complicate the device operation and poses a challenge for miniaturization.

Nanoporous silicon offers a unique solution to the above-mentioned challenges, by providing a material with large surface area to volume ratio that is ideal for capturing and concentrating a target analyte into a small volume. Provided the pore feature size is smaller than the optical wavelength, the resulting material behaves as an effective dielectric with optical properties that depend on the infiltrating substance. In comparison to evanescent sensors, the proposed device allows far greater overlap between the optical mode and the material to be sensed, thus enabling sensitive detection in a compact device, with a small analyte volume. The nanoscale porous structure prohibits fouling of the detector by larger particles. As we demonstrate here, the on-chip integration in a Mach-Zehnder interferometer (MZI) structure permits interferometric measurement while avoiding the problems of phase instability that plague free-space or fiber-based interferometers.

Several porous silicon sensor designs have been proposed and demonstrated. Many prior devices rely on observation of the reflection interference spectrum from porous structures, including single layers [6, 7], Bragg mirrors [8, 9] or resonant cavities [10–14]. Transmission measurements have also been achieved by measuring the change in birefringence when a free-standing porous substrate is filled with a solvent or analyte [15, 16]. All of these devices that utilize an optical path that is perpendicular to porous silicon substrate, and therefore inherently suffer from limited sensitivity because of the short interaction length. Further, many of them

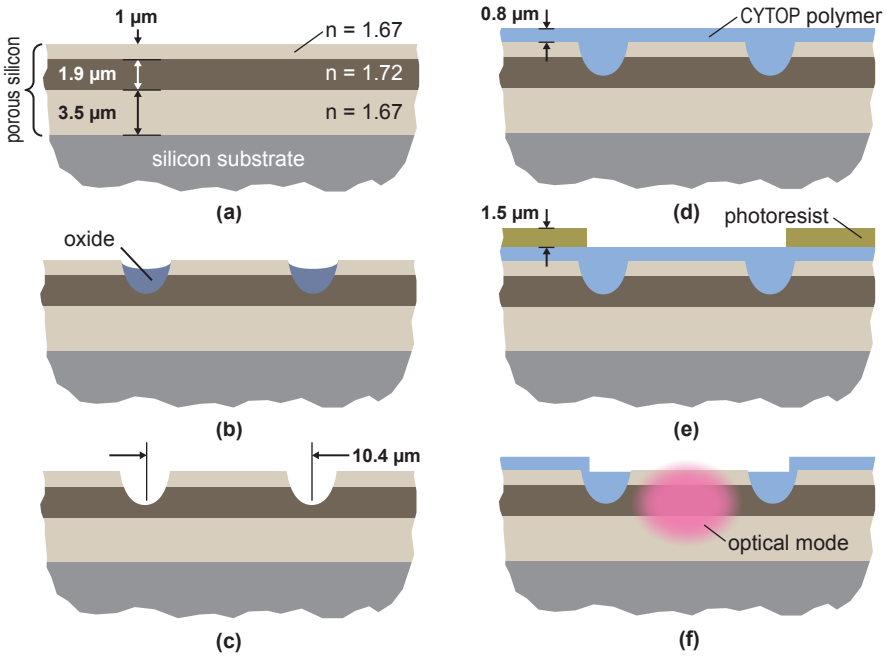

Figure 2.1: Fabrication process used to produce integrated porous silicon waveguides. (a) A three-layer planar waveguide is formed by electrochemical etching of crystalline silicon. (b) Two parallel lines are inscribed using direct-write laser oxidation, to form the left and right boundaries of the optical waveguide. (c) The oxidized regions are removed in a solution of dilute HF. (d) A planarizing polymer layer (CYTOP) is spin-coated over the structure. (e) The sensing window is photolithographically defined, and (f) reactive ion etching is used to expose the underlying porous silicon waveguide.

require a relatively wide-range tunable laser or broadband light source to detect shifts in the spectral pattern - a direct consequence of the large free-spectral range of thin dielectric films.

A solution to this issue is to employ a waveguide structure that confines light in two dimensions and guides parallel to substrate. This design allows relatively long interaction length by simply extending the length of sensing area. Vertical confinement of light in porous silicon can be easily achieved by controlling the etching current during fabrication, thus introducing high index guiding layer in between lower index cladding layers. Several recent studies used this multi layer core and cladding structure as a planar waveguide with coupling structures to increase sensitivity [38–42]. However waveguides that confine light in two dimensions require some transverse confinement structure in addition to a planar dielectric stack. Techniques to incorporate transverse confinement include lithographic patterning and dry etching of multi layers [43], masking of the crystalline silicon substrate prior to electrochemical etching [44–46], and direct laser oxidation of the surrounding regions, as we use here [47, 48].

Here we describe the fabrication and characterization of a single-mode porous silicon integrated MZI waveguide, with a polymer passivation layer used to restrict the analyte to a prescribed active sensing region. The device is fabricated using direct-write laser oxidation of a planar porous multilayer substrate, to produce a fully-confined optical waveguide. The functionality of the sensor is demonstrated using isopropyl alcohol as a test analyte, which is shown to produce a large, measurable phase shift, even when the exposed region is confined to be only 200 μm. We

compare the performance of the integrated MZI to a comparable fiber-based MZI, and show greatly improved stability.

2.1 Fabrication

2.1.1 Slab waveguide Fabrication

Figure 2.2 describes electrochemical etching cell used for fabricating porous silicon slab waveguide. The porous waveguide was fabricated by electrochemical etching of a p-doped (1-5 mΩ cm, $N \approx 10^{19}$ - 10^{20} cm^{-3}) $\langle 100 \rangle$ crystalline silicon substrate in a 25% hydrofluoric acid solution (hydrofluoric acid, water, ethanol 1:1:2 by volume). A three-layer buried-core slab waveguide was formed by applying current density of 98.4 mA/cm^2 for the core layer and 121.5 mA/cm^2 for top and bottom cladding layers, thereby introducing a 1.9 μm-thick intermediate core layer with refractive index of 1.72 between 1.0 μm top and 3.5 μm bottom cladding layers with refractive index of 1.67. The layer profile was chosen to minimize loss and ensure single mode operation in vertical direction. The etch rate was 60.4 nm/sec and 69.6 nm/sec for the core and cladding, respectively, and the etching durations were adjusted to achieve the desired thickness.

The etch rates and refractive indices were calibrated by performing optical reflectance and profilometry measurements on separately-fabricated single-layer samples as shown in figure 2.3. We fabricated 9 porous samples with current density ranging form 90 to 210 mA/cm^2 and etching time of 400 second. The reflectance spectrum from a single porous layer on the (reflective) silicon substrate was mea-

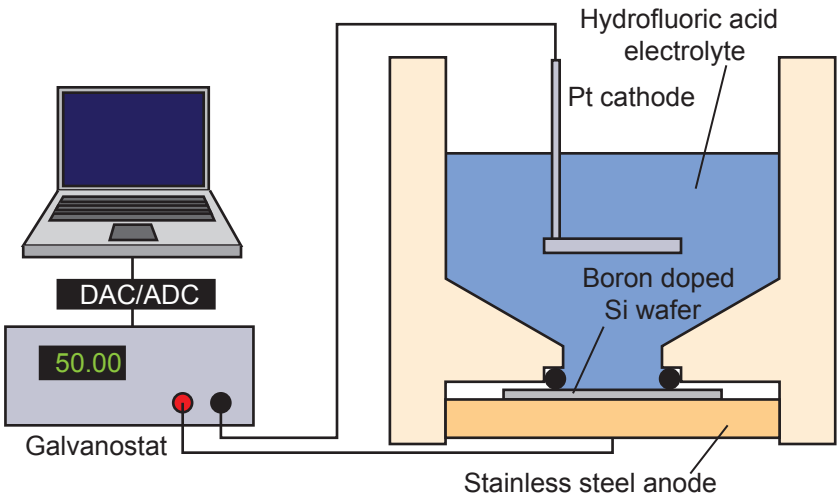

Figure 2.2: Electrochemical etching system used to fabricate nanoporous silicon devices

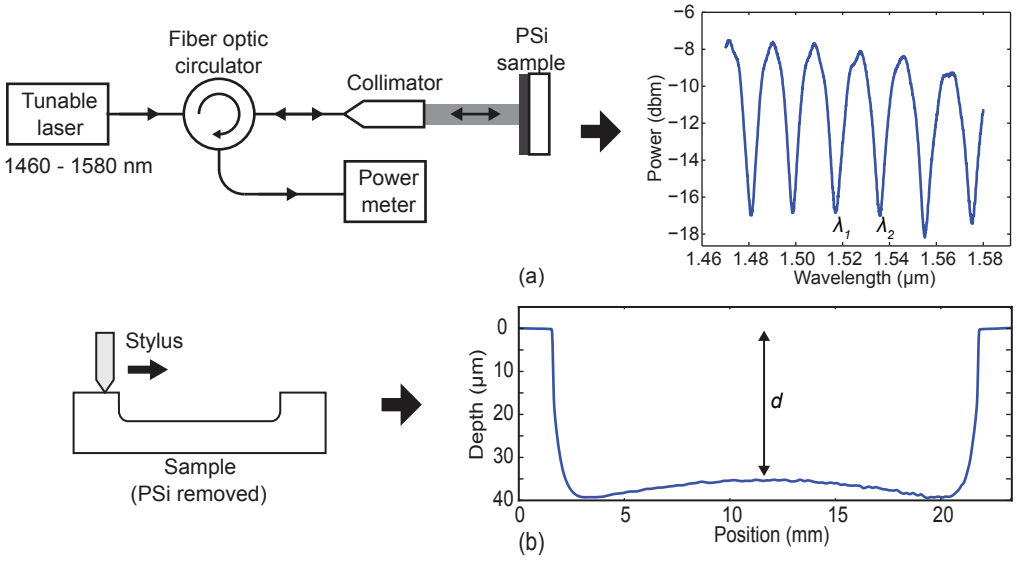

Figure 2.3: (a) Optical reflectance measurement and (b) profilometry measurement used to measure the refractive index and electrochemical etch rate, respectively.

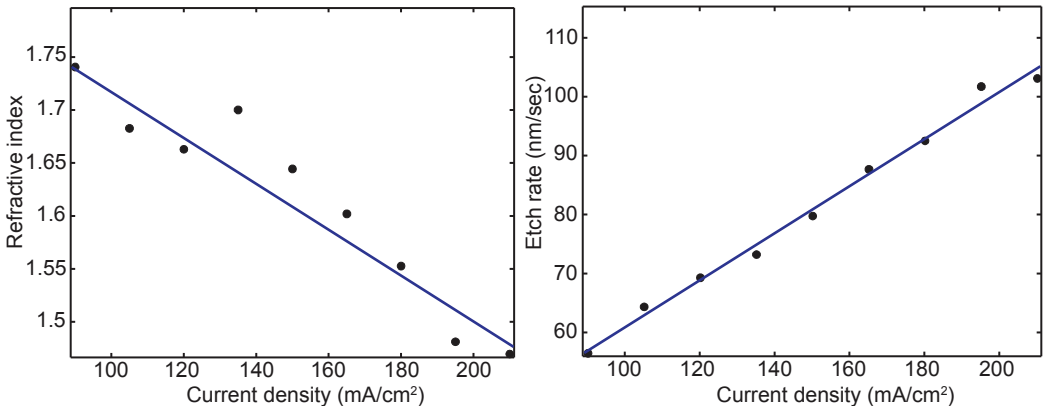

Figure 2.4: Refractive index vs. current density (left) and etch rate vs. current density (right) calibration result

sured using a tunable 1.55 μm laser, and the etch depth was subsequently measured by profilometry, after selectively removing the porous layer in a solution of sodium hydroxide (NaOH). The refractive indices and etch rate were then calculated from the period of the fringes observed in reflectance and depth measured from profilometry using equations below.

$$n = \frac{1}{2d}\frac{\lambda_1\lambda_2}{(\lambda_2 - \lambda_1)} \tag{2.1}$$

$$\text{etchrate} = \frac{d}{t} \tag{2.2}$$

where n is refractive index, λ_1 and λ_2 are adjacent minima wavelengths from reflectance measurement, d is depth from profilometry measurement and t is the etching time of the sample. Figure 2.4shows refractive index vs. current density (left) and etch rate vs. current density (right) calcualted from equation 2.1and 2.2. Within calibrated current density range, both refractive index and etch rate vary linearly as current density changes.

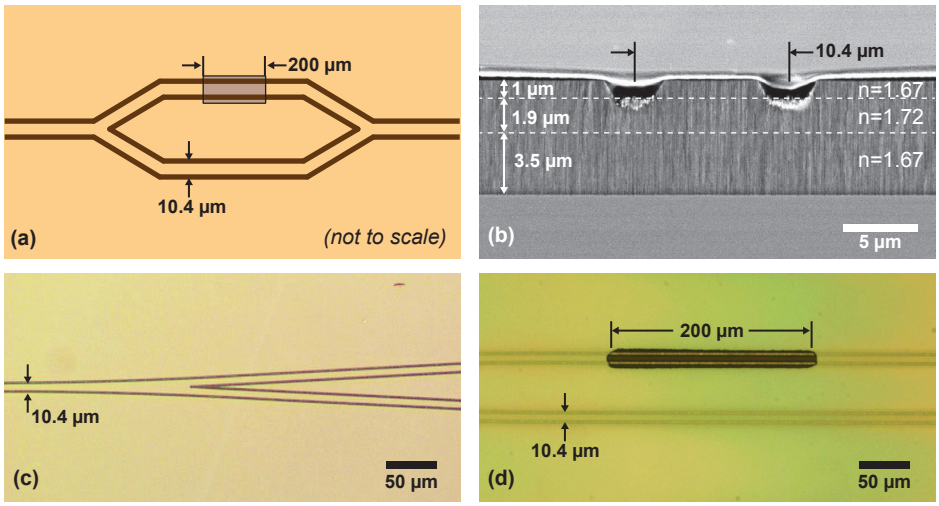

Figure 2.5: (a) Schematic of integrated MZI waveguide. (b) Cross-sectional scanning electron micrograph (SEM) of a single waveguide. (c) Optical micrograph of Y-branch. (d) Optical micrograph showing selectively exposed sensing window in one arm of the interferometer.

2.1.2 Channel waveguide

The slab waveguide only confines light in the vertical dimension. Lateral light confinement structure is necessary to make fully integrated waveguide devices such as slitters and interferometers. This structure was fabricated by selectively oxidizing porous silicon by focused laser beam. The scanning laser oxidation system is shown in figure 2.6. The resulting slab waveguide was placed on a programmable XY translation stage, and a 532 nm continuous-wave (CW) laser with power of 25 mW was focused onto the surface through a 40×, 0.66 NA microscope objective, while the substrate was scanned at a speed of 0.4 mm/s. The focused spot diameter is approximately 3 μm. The 532 nm illumination is strongly absorbed in the

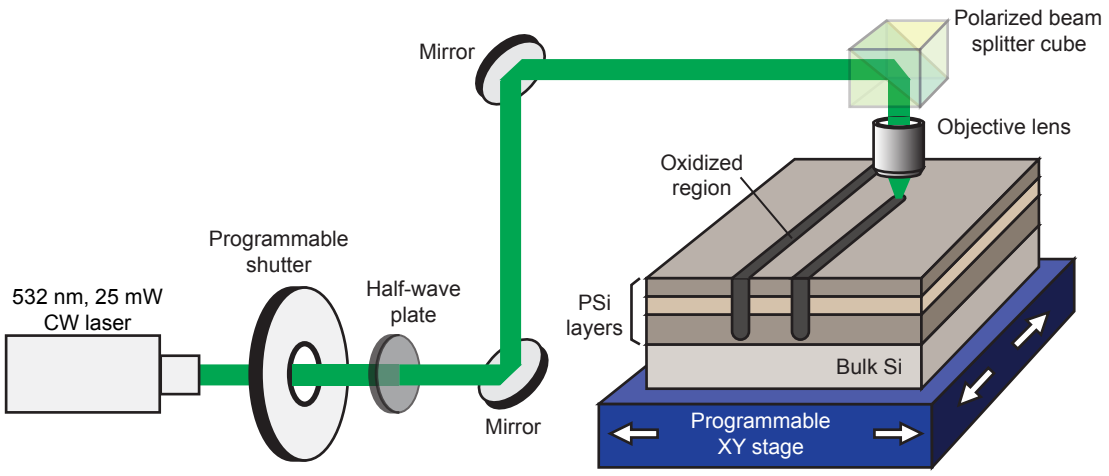

Figure 2.6: Scanning laser oxidation system

porous layer, which produces a localized region of oxidized porous silicon, which was later selectively removed using a dilute solution of hydrofluoric acid. The resulting structure was partially oxidized in a rapid thermal annealing (RTA) furnace at 400°C for 5 min. in order to passivate the silicon surface. Figure 2.5(b) shows the cross-sectional micrograph of a completed single-mode optical waveguide formed by inscribing two such parallel lines.

Lasers with three different wavelengths were tested to optimize the fabrication process. Cross-sectional views of oxidized channels by 473 nm, 532 nm and 980 nm lasers are shown in figure 2.7. 532 nm laser was chosen because the wavelength provides oxidation speed and depth required for fabrication process. Compared to 532 nm, 473 nm and 980 nm have disadvantages of shallow oxidation depth and slow oxidation speed, respectively.

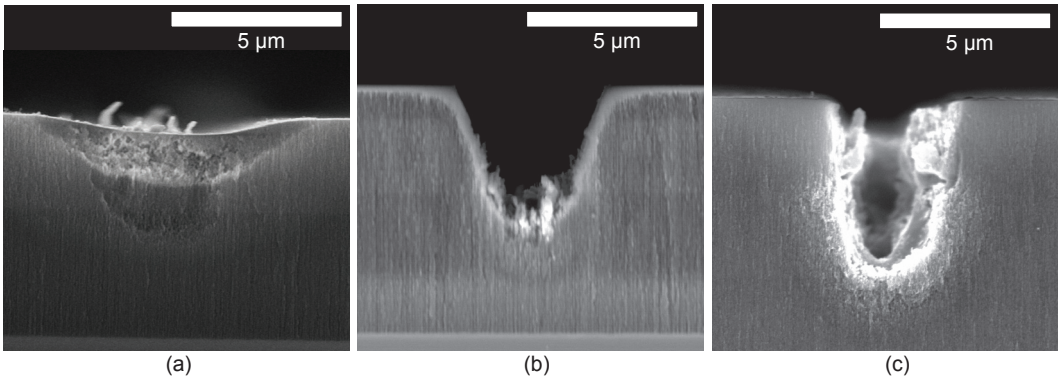

Figure 2.7: SEM micrographs of cross sectional view of grooves fabricated by (a) 473 nm, (b) 532 nm and (c) 980 nm.

2.1.3 Planarization and window etching

In order to controllably introduce the analyte to the sensor, the entire device surface should be covered except for a prescribed sensing area. Cytop polymer was used as a cover layer on top of device. Cytop (Asahi Glass Co.) is an optically transparent fluoropolymer with relatively low refractive index (n = 1.3) compared to other transparent polymer such as benzo cyclo butene (n = 1.54). The cover layer with smaller refractive index compared to porous silicon layers is important in order not to disrupt the waveguide propagation mode. Following fabrication of the waveguides, a low-index, 0.8 μm-thick Cytop layer was spin-coated onto the waveguide and cured, followed by a 1.5 μm-thick photoresist imaging layer. Immediately prior to spin-coating the photoresist, the Cytop layer was briefly exposed for 15 seconds in an oxygen plasma etcher, followed by application of hexamethyldisilazane (HMDS). Both steps were found to be effective in ensuring adequate adhesion of the photoresist layer. The photoresist was patterned using the same scanning laser

lithography system described above, with a 10×, 0.25 NA microscope objective and 473 nm, 0.5 mW laser to selectively expose a 200 μm long region above the sensing arm of the interferometer. Following development, the underlying polymer was removed through reactive ion etching in an oxygen plasma, revealing the porous waveguide underneath. Note that porous silicon is easily dissolved by alkaline solutions including resist developers. An additional protection layer, Cytop in this case, is necessary for photolithography process of porous silicon. After lithographic processing, the device was cleaved to allow edge-coupling at the input and output facets. Figure 2.5(c)-(d) presents top-down optical micrographs of the Y-branch waveguide and the 200 μm exposed sensor region.

2.2 Characterization

2.2.1 Single mode operation

In order to ensure a stable and equal power splitting ratio for the Y-branches that comprise the MZI, it is essential that waveguides support only a single optical mode. In order to confirm that the waveguide is singlemode, we used an infrared camera to monitor both the power and mode shape emerging from the output of a simple Y-branch waveguide. Figure 2.8 illustrates experimental setup for mode observation from waveguide's output facet. A 1550 nm laser was coupled into single-branch facet through a lensed fiber and the emerging beams from the double-branch facet was focused on a phosphor-coated CCD camera through a 20× objective. The relative brightness between the two waveguides was observed at the output facet

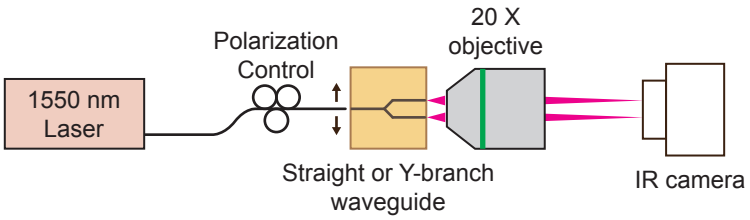

Figure 2.8: Experimental setup for observing optical modes from the output facet

while moving the lensed fiber position on input facet. When the waveguide width was smaller than 10.4 μm, the light was equally split between the two output waveguides, as shown in Fig. 2.9(a), even when the position of the input lensed fiber was adjusted, indicating that the waveguide is singlemode under these conditions. Conversely, for waveguides wider than 10.4 μm, the splitting ratio was observed to depend on the input coupling conditions indicating multimode behavior (Fig. 2.9(b)). Further measurements conducted on straight waveguides show that the output mode shape is independent of fiber position for the single-mode case (Fig. 2.9(c)), but depends strongly on the fiber position in the multimode case (Fig. 2.9(d)).

2.2.2 Loss measurement

The waveguide propagation loss was initially estimated by performing cutback measurements of the transmission for straight waveguides of three different lengths (figure 2.10). Cutback method is relatively quick and easy way to estimate propagation loss since it does not require extra sample processing step. However coupling efficiency may vary for each cleaving and fiber-waveguide aligning procedure. The input and output coupling losses were estimated by extrapolating the total insertion

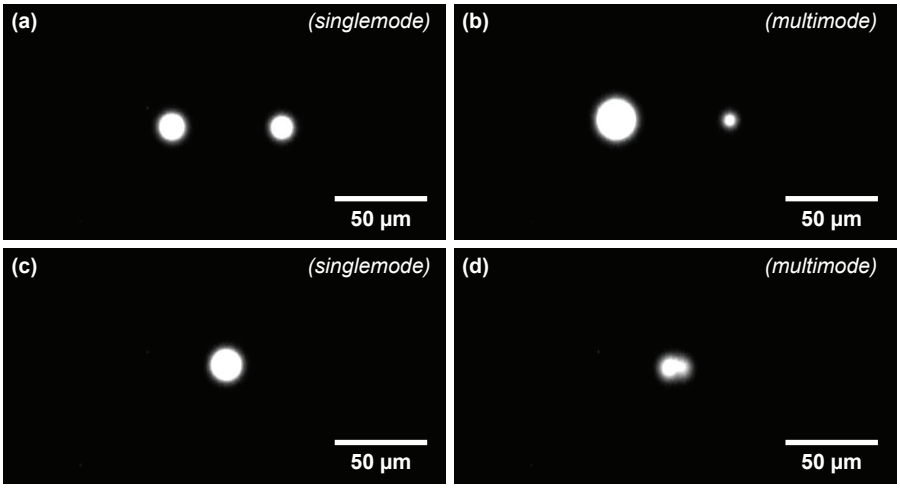

Figure 2.9: Observations of optical pattern emerging from porous silicon waveguide for (a) singlemode waveguide with y-branch, (b) multimode optical waveguide with y-branch, (c) singlemode straight waveguide and (d) multimode straight waveguide.

loss measurements to a device length of zero, and the excess scattering loss in the y-branch was calculated by comparing the total output power to that of a straight waveguide with the same length. The total waveguide insertion loss in a 12 mm long device was estimated to be 25 dB, including coupling loss (2 dB/facet), propagation loss (16 dB), and scattering loss in the y-branch (5 dB).

2.3 Experimental results

A fiber coupled 1550 nm continuous-wave laser with maximum power of 4 mW was coupled into input facet of MZI waveguide through a lensed fiber. The light emerging from the waveguide was collected with a second lensed fiber and photodiode, which records the interferometric signal, as illustrated in Fig. 2.11(a).

For comparison, we conducted measurements using a similarly fabricated straight

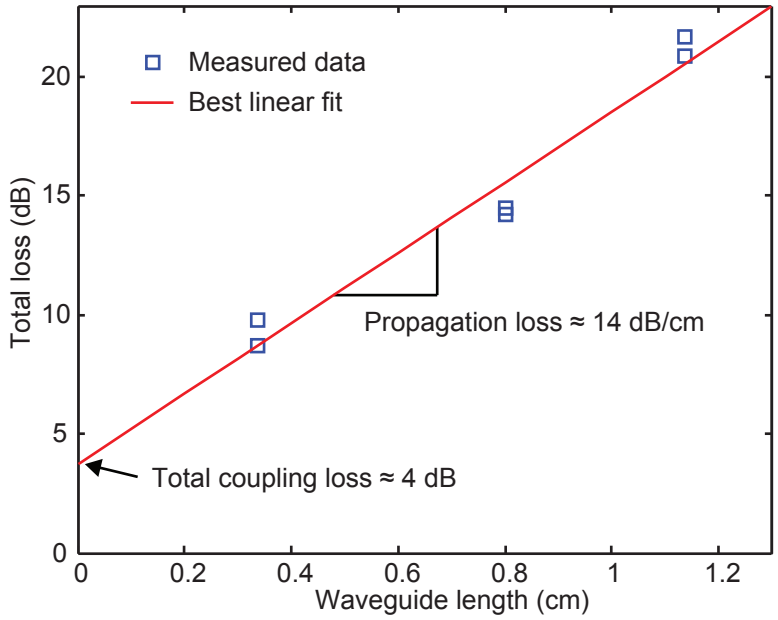

Figure 2.10: Propagation loss estimation by cutback measurement

waveguide incorporated into a fiber-optic MZI. In this experiment, the output from the laser was split using a 90:10 fused fiber coupler, with the 90% output directed through a straight porous waveguide, as shown in Fig. 2.11(b). The size of the sensing window was identical between the straight waveguide and the integrated MZI. The outputs were recombined in a second, 50:50 fused fiber coupler and connected to a photodiode. The fiber based measurements used single-mode (non polarization-maintaining) fiber, and therefore require a polarization controller and polarizer to ensure that the signals from the two arms of the interferometer remain co-polarized. By contrast, the integrated MZI shown in Fig. 2.11(a) maintains the polarization state in the two arms.

Finally, in order to clearly differentiate phase and amplitude changes, we also conducted optical heterodyne phase measurement with the same straight waveguide,

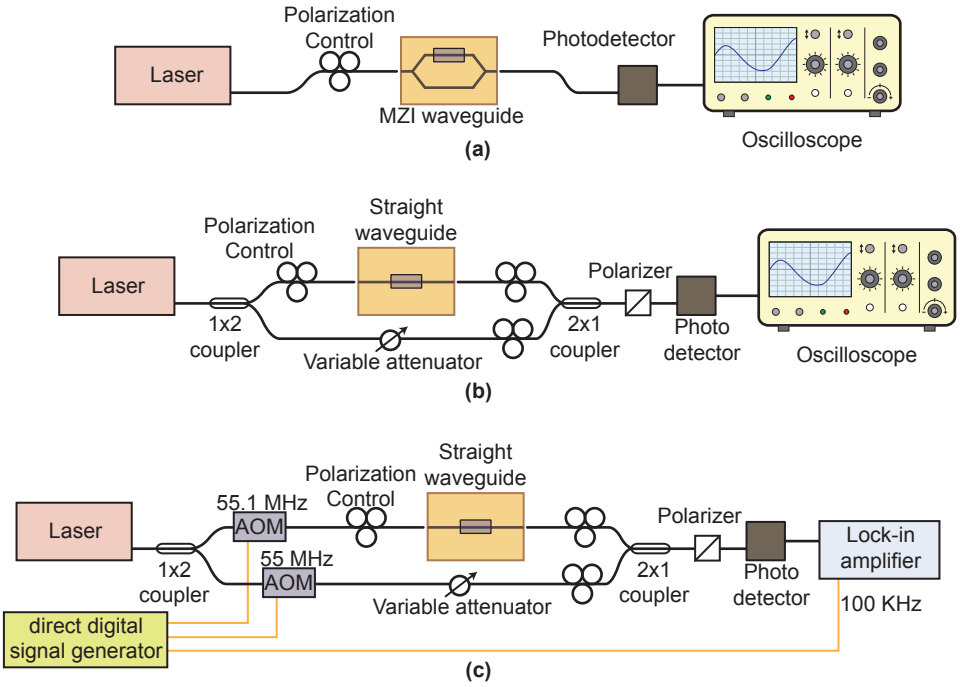

Figure 2.11: Experimental setups used to conduct interferometric porous waveguide measurements. (a) Integrated Mach-Zehnder interferometer (MZI) constructed using porous silicon waveguides. (b) Fiber-based MZI, with porous waveguide incorporated in one arm of interferometer, and (c) Heterodyne fiber-based interferometer, enabling simultaneous measurement of magnitude and phase shift in porous waveguide sensor.

using the system depicted in Fig. 2.11(c). Two acousto-optic modulators (AOM) were employed on both branches of fiber optic MZI, to shift frequency of sensing branch by 55.1 MHz and reference branch by 55.0 MHz. The magnitude of the resulting 100 kHz beat-signal was observed using a dual-phase lock-in amplifier with 100 kHz reference frequency. The relative phase and intensity of the optical signal is then translated into the magnitude and phase of the 100 kHz heterodyne signal.

2.3.1 Stability comparison between integrated MZI and fiber optic MZI

Figure 2.12 compares the stability between the integrated MZI shown in Fig. 2.11(a) and the corresponding fiber-based interferometer of Fig. 2.11(b), measured over a 400 second interval, when there is no analyte introduced to the sensor. To ensure an accurate comparison between the measurements, the optical powers were adjusted prior to the observation to ensure that both devices show full fringe contrast and have the peak output interferometric signal. The output of the MZI is nearly constant, indicating that the relative phase and intensity in the interferometer remains stable over the observation time. The fiber-based interferometer shows a significant slow drift of the output signal, associated with uncontrolled mechanical and thermal instabilities in the fiber and waveguide. In comparison to the fiber-based interferometer, the integrated MZI uses shorter arms that are integrated on the same chip in close proximity. Because the measurement responds only to the relative phase differ-

ence between the arms, any thermal and mechanical fluctuations that are common to the two arms will cancel, leading to the stable response observed in Fig. 2.12.

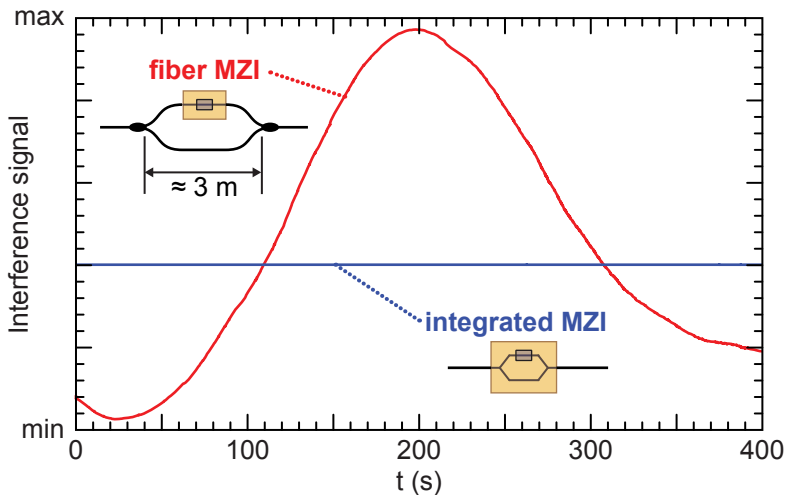

Figure 2.12: Comparison of stability from integrated porous Mach-Zehnder interferometer and fiber-based waveguide interferometer, conducted over 400 s with no analyte present. Prior to observation, both systems were adjusted to have full interferometric fringe contrast and equal fringe amplitude.

2.3.2 Sensor performance measurement

To demonstrate the sensor performance, we applied a drop of isopropanol to the active region of the waveguide using a micro-pipette, while observing the detected signal on an oscilloscope. Figure 2.13(a) plots the received signal from the integrated MZI device, measured over a 400 second interval during which the isopropanol was introduced. The enlarged plots in the lower panel below show the rapid phase shift (approximately 5 fringes over 2 seconds) that occurs when the analyte immediately penetrates the porous waveguide. This process later reverses

after about 200 seconds as the analyte evaporates out of the pores. A similar evolution is seen in the fiber-based interferometer, as shown in Fig. 2.13(b) but the response is superposed onto a slow, unrepeatable drift associated with thermal and mechanical instability of the fiber-based interferometer. The additional interference fringe in between penetration and evaporation seen in Fig. 2.13(b) is a consequence of the instability of the fiber-based interferometer, and does not reflect the true refractive index change caused by the analyte.

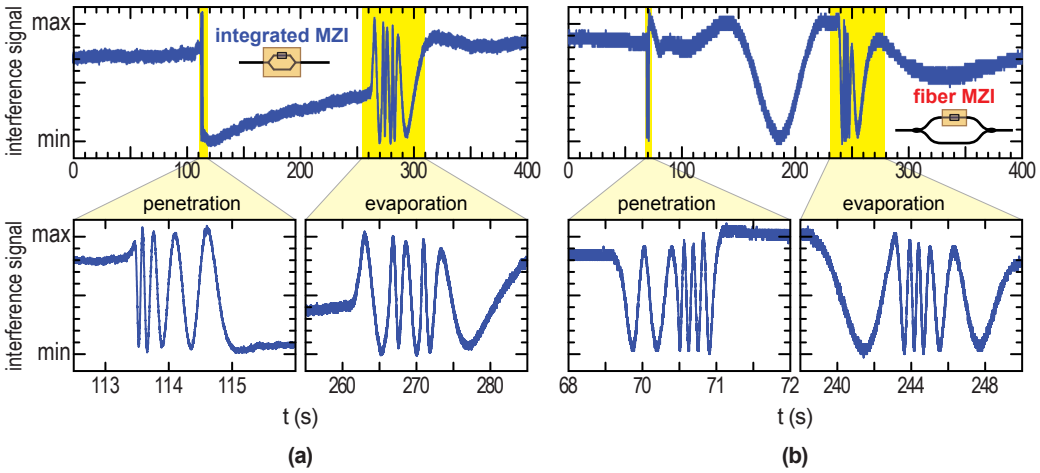

Figure 2.13: Interference signal measured from (a) integrated nanoporous silicon MZI device and (b) straight waveguide incorporated into an external fiber MZI. The interference signal is observed over a 400 s time interval during which a drop of isopropanol is introduced to the porous waveguide.

2.3.3 Heterodyne phase shift measurement

Figure 2.14 plots optical intensity and phase, measured using the fiber-based heterodyne system shown in Fig. 2.11(c). When the isopropanol penetrates the

waveguide, we see a rapid increase in the phase by approximately 9.7π, which agrees well with the fringe measurement obtained from the MZI. Upon evaporation, the phase shows a slower recovery to its original level.

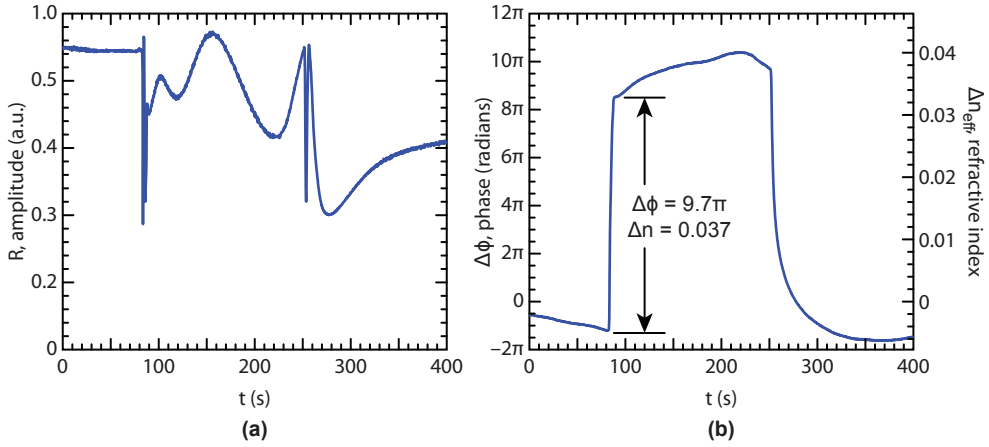

Figure 2.14: Heterodyne measurement of intensity and phase change from a 200 μm porous silicon waveguide that is exposed to isopropanol.

2.3.4 Sensitivity analysis

To estimate the sensitivity of the interferometric measurement, we relate the measured phase shift $\Delta\phi$ to the effective refractive index shift Δn_{eff} through the following relation:

$$\Delta n_{\text{eff}} = \frac{\Delta\phi\lambda}{2\pi L} \tag{2.3}$$

where λ is vacuum wavelength (1.55μm) and L is interaction length (200 μm). The right axis in Fig. 2.13(b) shows the calculated refractive index shift of the waveguide, which shows a reversible refractive index shift of 0.04 refractive index units (RIU) caused by the isopropanol. From Eq. 2.3, we estimate the sensitivity of 13,000

rad/RIU·cm. Assuming that the integrated MZI device has a limit of detection of 0.1 radian (5.7 degrees), a conservative estimate based on the data presented in Figs. 2.12 and 2.13, the device should be capable of detecting a refractive index change as small as 10^{-5} if the active area were increased to L = 1 cm.

Although the test analyte considered imparts a relatively large phase shift, the sensitivity estimated here is predicated on the assumption that the induced phase shift will be strictly proportional to the refractive index, as expressed in Eq. 2.3, even for smaller changes in the refractive index.

For comparison, the highest sensitivity porous silicon based optical sensors reported to date have used spectral measurements of resonant cavities [13]. These methods report a spectral sensitivity of 300-500 nm/RIU (meaning, for example, that with a spectral resolution of 0.1 nm, a refractive index shift as small as 2×10^{-4} could be detected.) By using prism or grating-based coupling into slab waveguides (with no transverse confinement), a sensitivity as high as 1000 nm/RIU has been reported [4, 42]. The integrated MZI reported here has the potential to exceed the sensitivity of existing approaches, in a simple device that is both stable and compact.

It should be acknowledged that the laser-based heterodyne interference measurement reported here, while more capable, is a more costly and sophisticated measurement than broadband reflectance spectrometry previously employed in planar porous silicon sensors [6–14]. However, the integrated MZI device could be easily modified by introducing an intentional path length difference between the arms, which would enable observation of interference fringes in transmission using broadband optical spectroscopy.

2.4 Summary

We describe the fabrication and measurement of an integrated nanoporous Mach-Zehnder interferometric waveguide sensor. Nanoporous silicon single mode integrated waveguides were successfully fabricated by electrochemical etching and direct-write laser oxidation. The nanoporous dielectric permits direct infiltration of the analyte gas or liquid into the waveguide core, enabling sensitive detection in a small device – thereby overcoming a key disadvantage of evanescent-mode sensors. Using isopropanol as a test analyte, we observed a phase shift of 9.7π in an interaction length as short as 200 μm. Sensitivity of 13000 rad/RIU-cm was measured which exceed most previous reports.

Chapter 3: Thermal conductivity of porous silicon

Thermal conductivity is one of the most important properties that affect performance of electrical and optical devices. Therefore accurate determination of a material's thermal conductivity is essential for properly designing such devices. Materials with nano scale structure, including porous silicon, exhibit quite different physical properties compared to their bulk or crystalline counterparts. A number of studies showed that porous silicon has thermal conductivity comparable to commonly used insulation materials such as SiO_2 or Si_3N_4 [49]. Also its thermal conductivity can be tailored during fabrication process. We investigated porous silicon's thermal conductivity using an electrical AC heating method (3-ω method). The method provide a simple way of measuring thermal conductivity of materials in bulk or thin film form. Moreover, the 3-ω method can be used to measure the anisotropy in the thermal conductivity, which is discussed in following chapter.

3.1 Prior thermal measurement of porous silicon

Porous silicon's thermal conductivity was studied by several different methods. The first measurement result of porous silicon's thermal conductivity was reported by Lang and co-workers using the thermal wave propagation. Later, 3-ω, micro-

Raman, photo-acoustic and scanning thermal microscopy methods were used to measure the thermal conductivity. The list of prior studies are shown on table 3.1. All of them reported that the thermal conductivity of porous silicon is 2-3 orders of magnitude smaller than crystalline silicon.

Table 3.1: Previously reported thermal conductivity of porous silicon

Authors	Year	Methods	Sample type	k ($Wm^{-1}K^{-1}$)
W. Lang *et al.* [50]	1994	Thermal wave propagation	p, n p+	1.2 - 1.8 80 as prepared 2.7 oxidized
G. Gesele *et al.* [26]	1997	3-ω	p+(0.01 Ω·cm) p(0.2 Ω·cm)	0.8 at room temp. 0.2 at room temp.
S. Périchon *et al.* [22]	1999	Micro-Raman	p+	1
V. Lysenko *et al.* [23]	1999	Micro-Raman	p+(0.01 Ω·cm)	0.36 - 4.6
S. Périchon *et al.* [24]	2000	Micro-Raman	p+	0.3 - 0.7
U. Bernini *et al.* [20]	1999	Photo-acoustic	n(1 Ω·cm)	1.2 - 3.5
U. Bernini *et al.* [21]	2003	Photo-acoustic	n(1 Ω·cm)	0.29 - 2.93
S. Gomès *et al.* [25]	2007	Scanning thermal microscopy	p+(0.01 Ω·cm)	1.7 - 3.8

3.2 3-ω method

The 3-ω method has been widely used to measure thermal conductivity of materials. It utilizes a metal strip deposited on top of the sample functioning as a heater and temperature sensor. An electrical current at frequency of 1-ω is applied across strip and generate sinusoidal heating at 2-ω. Because the resistance of metal varies linearly with temperature, heater resistance oscillates at 2-ω. The resulting voltage across the heater becomes product of 1-ω current and 2-ω resistance which contains both 1-ω and 3-ω components. The 3-ω component measured across the

metal strip contains information of amplitude of temperature oscillation that is related to the thermal conductivity of the sample.

3.2.1 3ω voltage and temperature oscillation

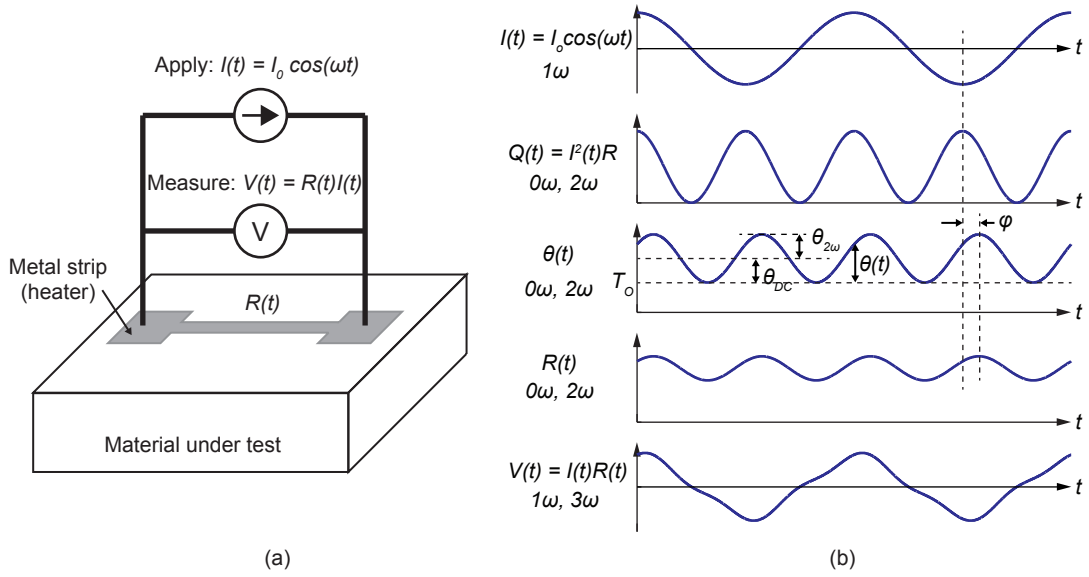

Figure 3.1: (a) Simplified 3-ω measurement diagram. (b) Relationship between current, heat power, temperature, electrical resistance and voltage.

Figure 3.1 illustrates the simplified diagram of 3-ω measurement and the relationship between the applied current, heat power, temperature, electrical resistance and measured voltage. A sinusoidal current $I(t)$ with frequency ω is applied to metal strip which generates Joule heat $Q(t)$ at frequency 2ω.

$$I(t) = I_0 \cos(\omega t) \tag{3.1}$$

$$Q(t) = I^2(t) R_e(t) \tag{3.2}$$

The heater resistance R_e is given as

$$R_e(t) = R_{eo}(1 + \alpha\theta(t)) \tag{3.3}$$

where R_{eo} is electrical resistance of heater at room temperature, α is temperature coefficient of resistance and $\theta(t)$ is temperature rise of heater $(T(t) - T_o)$. Since α of most metals are in the order of 10^{-3} K^{-1} and $\theta(t)$ is usually kept small ($\theta(t)$ <1 K), $R_e(t)$ can be approximated to R_{eo}. Therefore, Q can be written as

$$Q(t) = I^2(t)R_{eo} = \frac{1}{2}I_o^2 R_{e0}(1 + \cos(2\omega t)) \tag{3.4}$$

Now, $Q(t)$ can be divided into DC and 2ω parts

$$Q(t) = Q_{DC} + Q_{2\omega}(t) \tag{3.5}$$

$$Q_{DC} = \frac{1}{2}I_o^2 R_{e0}$$

$$Q_{2\omega} = \frac{1}{2}I_o^2 R_{e0}\cos(2\omega t)$$

Average value of $Q_{2\omega}$ is 0 at steady state. Therefore Q_{DC} is average heat flow over time. Since electrical resistance of metal strip varies linearly proportional to temperature, AC-steady state resistance can be expressed as

$$R_e(t) = R_{eo}(1 + \alpha\theta_{DC} + \alpha\theta_{2\omega}\cos(2\omega t + \phi)) \tag{3.6}$$

where θ_{DC} is temperature rise by Q_{DC}, $\theta_{2\omega}$ is amplitude of temperature oscillation by $Q_{2\omega}$ and ϕ is phase difference between applied current and temperature response of metal strip. Eventually, the voltage across metal strip, $V(t) = I(t)R_e(t)$, is found to contain spectral components at ω and 3ω.

$$V(t) = I(t)R(t) = I_0 R_{eo}\left(\cos(\omega t) + \alpha\theta_{DC}\cos(\omega t) + \frac{\alpha\theta_{2\omega}}{2}\cos(\omega t + \phi) + \frac{\alpha\theta_{2\omega}}{2}\cos(3\omega t + \phi)\right) \tag{3.7}$$

$$V_\omega(t) = I_o R_{eo}\left(\cos(\omega t) + \alpha\theta_{DC}\cos(\omega t) + \frac{\alpha\theta_{2\omega}}{2}\cos(\omega t + \phi)\right) \tag{3.8}$$

$$V_{3\omega}(t) = \frac{1}{2} I_o R_{eo}\alpha\theta_{2\omega}\cos(3\omega t + \phi) \tag{3.9}$$

Equation 3.9 shows that the amplitude of $V_{3\omega}$ is directly proportional to the amplitude of the temperature oscillation of metal strip $\theta_{2\omega}$. By rewriting $V_{3\omega}$, real and imaginary parts are separable.

$$V_{3\omega}(t) = \frac{1}{2} I_o R_{eo}\alpha\left(\theta_{2\omega}\cos\phi\cos(3\omega t) - \theta_{2\omega}\sin\phi\sin(3\omega t)\right) \tag{3.10}$$

$$\mathrm{Re}\{V_{3\omega,rms}\} = \frac{1}{2} I_{rms} R_{eo}\alpha\mathrm{Re}\{\theta_{2\omega}\} \tag{3.11}$$

$$\mathrm{Im}\{V_{3\omega,rms}\} = -\frac{1}{2} I_{rms} R_{eo}\alpha\mathrm{Im}\{\theta_{2\omega}\} \tag{3.12}$$

RMS values are introduced in the equations above because these reflect what is actually measured by a lock-in amplifier. Using equation 3.11 and 3.12, in-phase and out-of-phase components of temperature oscillation amplitudes are calculated.

3.2.2 Temperature oscillation of line heater on semi-infinite substrate

The simplest 3-ω sample geometry is line heater deposited on semi-infinite substrate as described in figure 3.2. This geometry is commonly used to measure thermal conductivity of isotropic bulk materials, and is the basis of other variations of the 3-ω method introduced later in this chapter that for characterizing thin film materials on a substrate. An expression for temperature inside the substrate was derived from heat diffusion equation in cylindrical coordinate with semi-infinite substrate and infinitely narrow heater approximations [27, 51]. By ignoring heat loss by convection, the temperature oscillation amplitude at distance $r = (x^2 + z^2)^{1/2}$ is

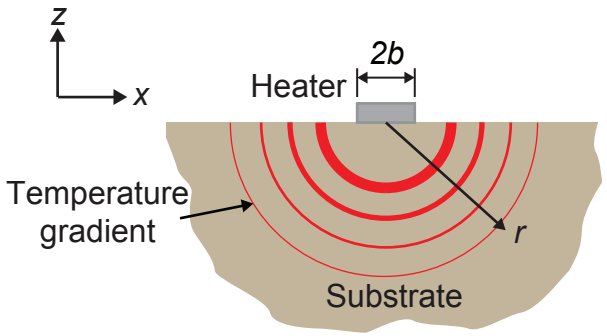

Figure 3.2: Line heater on semi-infinite substrate model

given by

$$\theta_{2\omega}(r) = \frac{P_{rms}}{\pi L k} K_0(qr) \tag{3.13}$$

Where P_{rms} is average power (heat flow) on heater, L is heater length, k is thermal conductivity of substrate material, $K_0(\cdot)$ is zeroth order modified Bessel function of second kind, $1/q = \sqrt{D/i2\omega}$ is thermal wavelength (or diffusion length) and D is thermal diffusivity.

Because the 3-ω method measures the heater temperature, we take $z = 0$ and replace $r = x$. In real experiment, heater has finite width, $|x| \leq b$. In this case, $\theta_{2\omega}(x)$ is derived by convolution with rectangular function. This operation can be accomplished by taking the Fourier transform.

$$\theta_{2\omega}(\xi) = \int_0^\infty \theta_{2\omega}(x)\cos(\xi x)\mathrm{d}x = \frac{P_{rms}}{2Lk}\frac{1}{\sqrt{\xi^2+q^2}} \tag{3.14}$$

where ξ is the Fourier wavenumber. Then apply convolution with rectangular function ($rect(x) = 1$ for $|x| \leq b$, otherwise 0), which gives

$$\theta_{2\omega}(\xi) = \frac{P_{rms}}{2Lk}\frac{\sin(\xi b)}{\xi b\sqrt{\xi^2+q^2}} \tag{3.15}$$

By taking inverse transform, we obtain

$$\theta_{2\omega}(x) = \frac{P_{rms}}{\pi Lk} \int_0^\infty \frac{\cos(\xi x)\sin(\xi b)}{\xi b\sqrt{\xi^2 + q^2}} \mathrm{d}\xi \tag{3.16}$$

The heater is usually made of a metal that is much more thermally conductive than the substrate. In this case, the temperature across heater quickly reaches an equilibrium state in which the temperature across the heater is uniform. By taking average of $\theta_{2\omega}(x)$ across heater, the average temperature oscillation amplitude on heater becomes,

$$\theta_{2\omega} = \frac{P_{rms}}{\pi Lk} \int_0^\infty \frac{\sin^2(\xi b)}{(\xi b)^2\sqrt{\xi^2 + q^2}} \mathrm{d}\xi \tag{3.17}$$

This is exact solution for $\theta_{2\omega}$ of metal strip. There is no closed-form analytic solution for this integration. However, the solution can be simplified by making some reasonable assumption. For the regime that thermal wavelength is much larger than heater width ($1/q \gg b$), the integration is dominated by value of ξ such that $q < \xi < 1/b$. In addition, an approximation applies for small b as below.

$$\lim_{b\to 0} \frac{\sin(\xi b)}{\xi b} = 1 \tag{3.18}$$

With this approximation, the solution simplifies to

$$\theta_{2\omega} = -\frac{P_{rms}}{2\pi Lk} \left[\ln 2\omega + \ln \frac{ib^2}{D} + \mathrm{const}\right] \tag{3.19}$$

The real part of this solution is seen to be a linear function of $\ln 2\omega$. This simplified solution indicates that amplitude of the real (in-phase) part of the temperature oscillation is a linear function of $\ln 2\omega$. The thermal conductivity can be generally estimated by plotting $\mathrm{Re}\theta_{2\omega}$ vs 2ω on a semi-log scale, and finding the slope. Theoretically, it is possible to calculate thermal conductivity from imaginary part of

solution. However it is mentioned by Cahill that slope method tend to be more accurate in real experiment [27]. $V_{3\omega,rms}$ which is measured is related to $\theta_{2\omega}$ by equations 3.11 and 3.12. By sweeping driving frequency ω in appropriate range and measuring $V_{3\omega,rms}$, the entire solution for $\theta_{2\omega}$ as a function of $\ln 2\omega$ can be acquired.

$$\theta_{2\omega} = \frac{2V_{3\omega,rms}}{I_{rms}R_{eo}\alpha} = -\frac{Q_{rms}}{2\pi Lk}\left[\ln 2\omega + \ln\frac{ib^2}{D} + \text{const}\right] \tag{3.20}$$

If experimentally measured slope of $\theta_{2\omega}$ vs. $\ln 2\omega$ plot is given as S, substrate thermal conductivity k is expressed as

$$k = \frac{P_{rms}}{2\pi LS} \tag{3.21}$$

3.3 Differential 3-ω method

The method described in previous section is only applicable in bulk or relatively thick material. It is convenient and useful to be able to measure thermal conductivity with thin film because it is challenging for some materials to be prepared in bulk form. Also, thin films often exhibit quite different thermal conductivity from their bulk counterparts as interfacial resistance becomes more prominent. The differential 3-ω method described in this section allows one to measure the thermal conductivity, especially cross-plane component, of a thin film on a substrate. The basic concept of this method is to assume that the thin film is a one-dimensional thermal resistor that transfers heat from the metal strip to the substrate. The thermal conductivity is determined from the temperature difference across the film. Details of the differential 3-ω measurement and analysis method will be discussed in this section. Also, limitations and several aspects that need consideration will be

discussed.

3.3.1 1-dimensional thermal resistor model

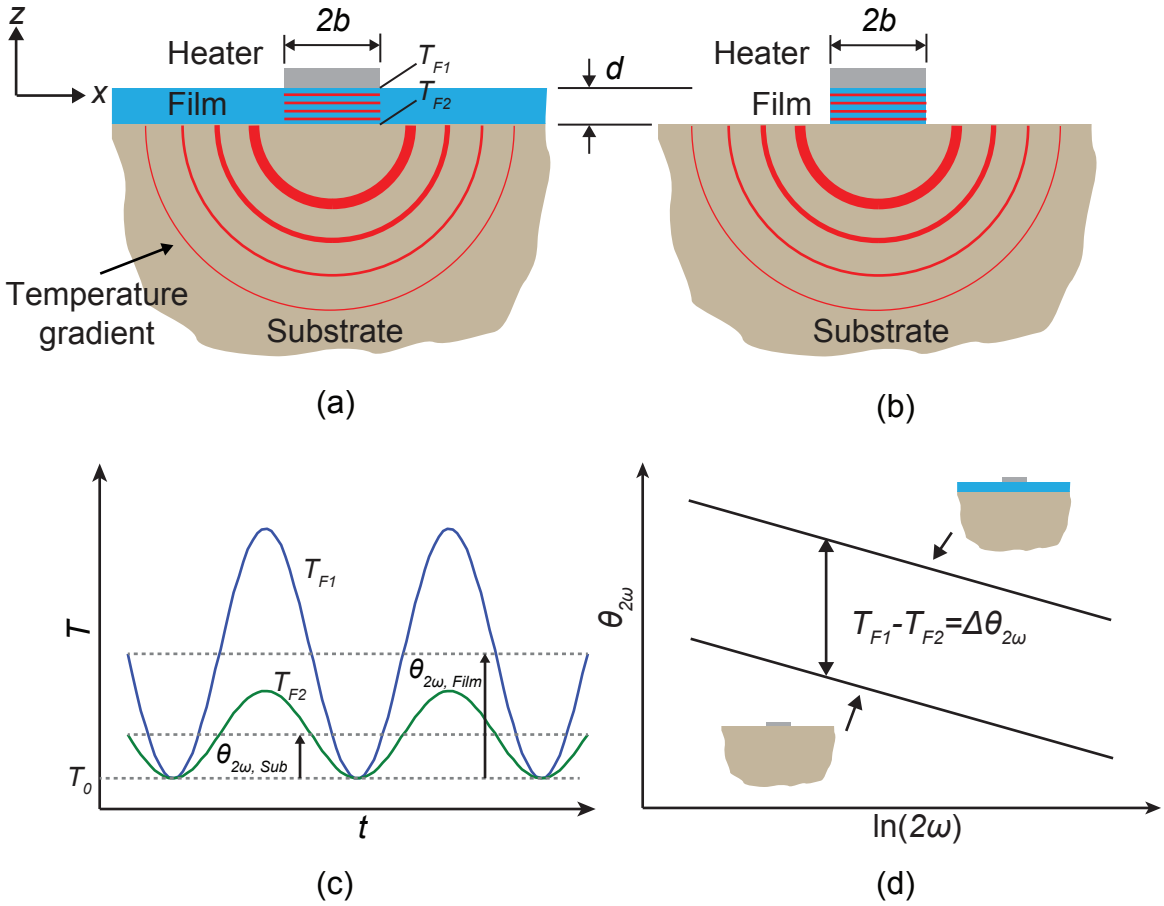

Figure 3.3: (a) Temperature gradient (heat flow) inside a typical 'thin film on substrate' sample for differential 3-ω measurement. (b) Ideal sample structure (micro-mesa) for differential 3-ω measurement. (c) Temperature oscillation of top and bottom interfaces of the film in time domain. (d) Amplitude of temperature oscillation of the two differential 3-ω measurement samples

In differential 3-ω method, the thin film is assumed to be a simple 1-dimensional

thermal resistor with cross-sectional area same as heater and length of film thickness. Figure 3.3 (a) illustrates the heat conduction in the typical differential 3-ω measurement sample. In a real sample, there is heat spreading at the edge of the heater, which violates the 1-dimensional thermal resistor assumption. The assumption can be satisfied by making the heater width much bigger than the film thickness ($b \gg d$), thus the relative amount of heat spreading gets negligible. If possible, the miro-mesa structure shown on figure 3.3 (b) is an ideal solution. Cross-plane component of the thermal conductivity,$k_{Film,z}$, can be derived by measuring temperature difference across the film. In steady state, thermal resistance of film is expressed as

$$R_t = \frac{d}{2k_z bL} = \frac{T_{F1} - T_{F2}}{Q} \tag{3.22}$$

where d, b and L are known dimensional values of sample, and Q is average heat flow through the thermal resistor. T_{F1} and T_{F2} are average temperatures on top and bottom surface of the thin film, respectively.

3.3.2 Temperature difference measurement

T_{F1} and T_{F2} are measured from two separate samples by ordinary 3-ω method. T_{F1} is measured from actual sample with thin film to be measured, and T_{F2} is measured from a substrate sample without thin film, otherwise identical to first sample. If measured values are given as $\theta_{2\omega,Film}$ and $\theta_{2\omega,Sub}$, R_t is rewritten as following in quasi-DC regime.

$$R_t = \frac{d}{2k_{Film,z} bL} = \frac{\theta_{2\omega,Film} - \theta_{2\omega,Sub}}{P_{rms}} \tag{3.23}$$

Therefore, $k_{Film,z}$ is expressed as

$$k_{Film,z} = \frac{d}{2bL} \frac{P_{rms}}{\theta_{2\omega,Film} - \theta_{2\omega,Sub}} \tag{3.24}$$

Measuring T_{F1} and T_{F2} for a range of ω is commonly done instead of temperature at fixed frequency. The distance between two functions represents the temperature difference across the film. Figure 3.3 (c) illustrates schematically the temperature oscillation on heater (T_{F1}) and film-substrate interface (T_{F2}) in time domain, and two differential samples' $\theta_{2\omega}$ as linear functions of $\ln(2\omega)$ shown on figure 3.3 (d).

3.4 Instrumentation

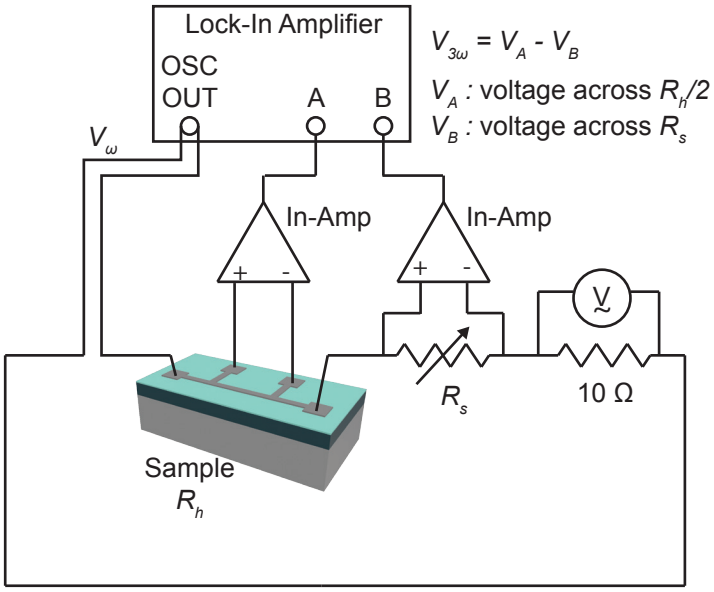

Figure 3.4: Diagram of 3-ω thermal conductivity measurement setup

Figure 3.4 shows schematic diagram of 3-ω measurement setup. A lock-in amplifier (Signal Recovery 7270) was used as both a signal source and measurement

instrument. The lock-in amplifier is capable of simultaneously measuring signals at two harmonics of the reference frequency. Sinusoidal signal at angular frequency 1-ω from internal oscillator drives heater circuit while the lock-in amplifier simultaneously measures the voltage signals at 1-ω and 3-ω. The measurement sample was placed on a large aluminum block with highly heat conductive paste on back side to allow for heat dissipation. The aluminum block has heat capacity much higher than sample, therefore heat generated from heater quickly dissipated into the block thereby maintaining the sample at room temperature. The sample temperature is monitored by K-type thermocouple connected at the edge of sample. Sample was connected to the rest of experimental circuit by four microprobes.

If internal oscillator generates pure sinusoidal signal at frequency 1-ω, the 3-ω signal across heater would be solely induced by temperature oscillation. However, signal from internal oscillator was found to have significant harmonic distortion at 3-ω frequency that corrupts the measurement. The problem can be resolved by introducing differential measurement technique that cancels out common noise by introducing series resistor. Because the series resistor does generates negligible heat compared to the sample, the voltage across the resistor is always proportional to applied signal. Voltages across the sample and series resistor are differentially recorded using the inputs A and B of the lock-in amplifier. Instrumentation amplifiers are required on both sides to isolate the heater circuit from lock-in amplifier's signal acquisition circuit. In order to match amplitude of the common signal on both input, the series resistor was adjusted so that ω component of $V_A - V_B$ is zero. The 3-ω component of $(V_A - V - B)$ then reflects only the thermal heating of the

measurement sample, with the harmonic distortion, which is common to both channels, subtracted out. The internal oscillator frequency ω is computer controlled and swept. A 10 Ω resistor is employed in series with the heater and series resistor to monitor current in circuit using an oscilloscope.

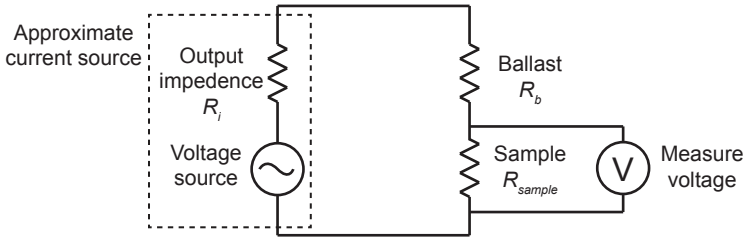

Figure 3.5: Schematic diagram of 3-ω measurement circuit with approximate current source

Ideally, the sinusoidal signal that drive heater circuit is intended to be a current signal. The best option is using commercial sinusoidal current source. Another option is to use a voltage-to-current circuit that convert voltage signal produced by the lock-in amplifier into a current signal. The easiest solution is to simply use the voltage source such as lock-in amplifier's oscillator output as an approximate current source. This can be achieved by using a series ballast resistor with relatively high resistivity compared to heater (figure 3.5). If ballast resistor's resistivity is comparable to heater, correction factor is available [28].

$$\theta_{true} = \theta_{apparent}\left(1 - \frac{R_{sample}}{R_{total}}\right)^{-1} \tag{3.25}$$

where $R_{total} = R_i + R_b + R_{sample}$ (see figure 3.5).

3.5 Sample fabrication and characterization

3.5.1 Fabrication

The fabrication process used to produce the measurement samples is illustrated in figure 3.6 (a)-(d). The porous silicon layer was formed by electrochemical etching of boron doped (p-type), ⟨100⟩ silicon substrate, using the process described in chapter 2. As described in previous chapter, porosity increase as etching current density increases. Also, porous silicon etched from substrate with relatively lower doping density exhibits smaller pore size compared to porous silicon on highly doped substrate. Samples with several different combinations of substrate doping density and porosity were prepared to investigate their effects on thermal conductivity. Silicon substrate with two different range of electrical resistivity (0.1 Ω·cm and 0.001 Ω·cm) are used. Porous silicon layers with thickness of 1 μm and 2 μm are formed on both substrates. For each thickness, two different porosity samples are prepared (Characterized by nominal refractive index of 1.7 and 1.8 respectively, according to etching calibration data). On top of porous silicon layer, 200 nm of SiO_2 layer was deposited by PECVD process to prevent electrical short between heater and porous silicon layer. After SiO_2 deposition, standard positive photoresist was spin coated to pattern metal heater. Photoresist was exposed by laser lithography system described in previous chapter. Followed by development, 200 nm of aluminum was deposited by thermal evaporation, than excessive resist and aluminum was lifted off by resist stripper. Figure 3.6 (e) shows heater design that is patterned on top

of samples. The heater width ($2b$) of 30 μm was chosen to satisfy the 1D thermal resistor assumption. Because the 2- dimensional, semi-cylindrical heat flow model does not apply at both end of heater, near the contacts, we use only center region of heater for measurement. Heater was designed in such a way that center half length is used to measure voltage signal while current is driven across full length. Figure 3.6(f) illustrates cross sectional view of completed sample.

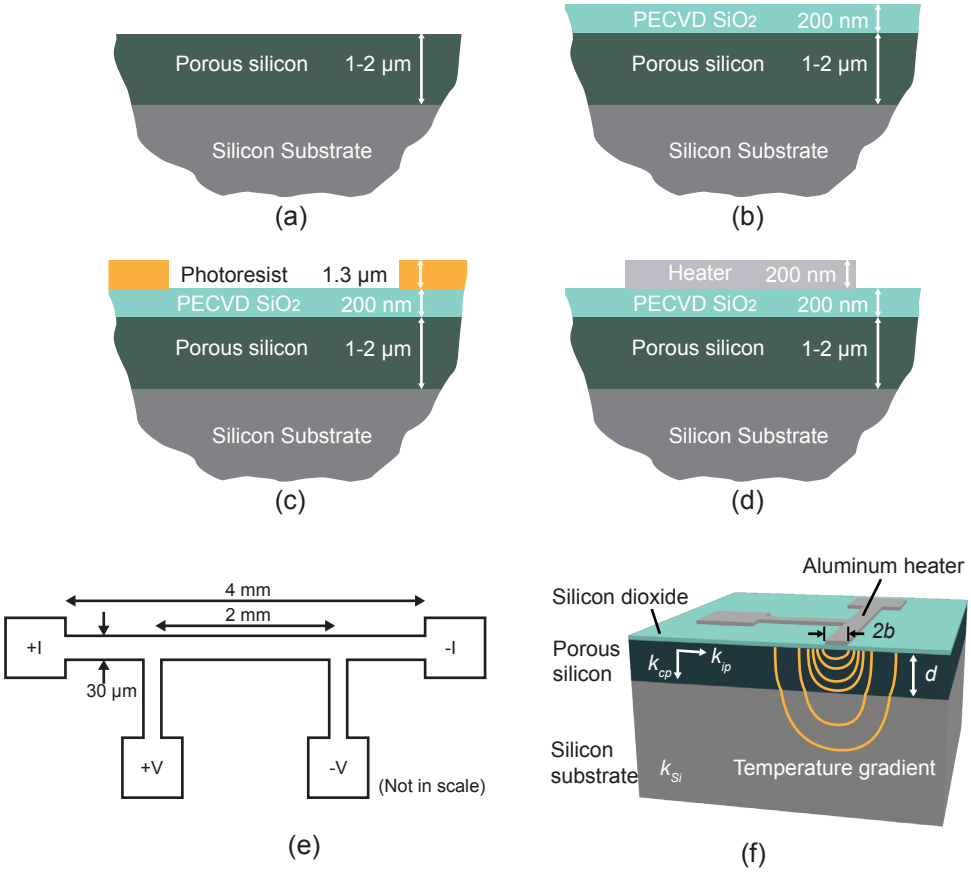

Figure 3.6: 3-ω sample fabrication process. (a) Porous silicon layer is formed by electrochemical etching. (b) PECVD SiO_2 is deposited for electrical insulation. (c) Photoresist is spin-coated and patterned. (d) 200 nm Aluminum is deposition and excessive area is lifted-off. (e) Heater design (f) Completed sample

3.5.2 Resistance thermometry

Since 3-ω method rely on electrical resistance change with temperature (e.g. equation 3.3), measuring temperature coefficient of resistance, α, is important for accurate measurement. It is possible to use known value of α for the material comprising the heater. However α of thin film is often different form bulk value and also depends on deposition method. α was measured by a standard 4-probe technique with the sample on a hot plate. Sample was placed on hot plate with heat conductive paste. Thermocouple is placed on top surface of sample to monitor temperature. The heater and a 10 Ω resistor were connected to DC power supply in series. The 10 Ω resistor was used to monitor current in circuit. The sample was heated to 70°C, and than the voltage across heater and standard resistor were monitored by multimeters while temperature drops. The heater resistance at each temperature is expressed as

$$R_{heater} = \frac{R_s V_{heater}}{V_s} \tag{3.26}$$

where R_{heater} is the heater resistance, R_s and V_s are the resistance and voltage across series resistor and V_{heater} is voltage across the heater. dR/dT is derived from R vs. T plot. The temperature coefficient of resistance is given as

$$\alpha = \frac{1}{R_{heater,room}} \frac{dR}{dT} \tag{3.27}$$

R vs. T plot of heater is shown on figure 4.5. In temperature range of measurement, resistance varies linearly by temperature. α from measurement was 3.17×10^{-3} K^{-1} which is slightly different from known value of aluminum ($3.8 - 4.3 \times 10^{-3}$ K^{-1}).

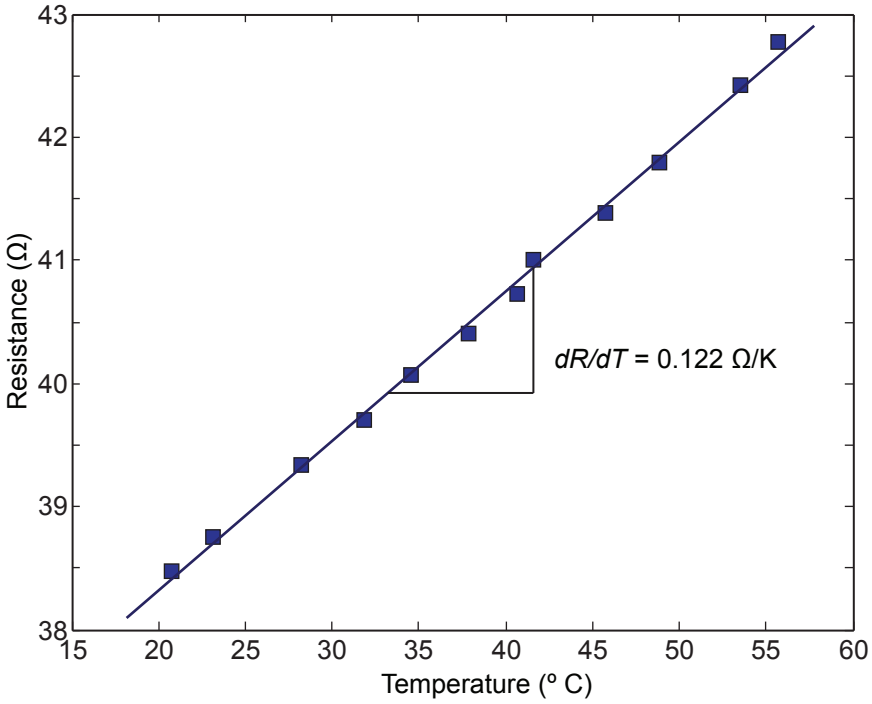

Figure 3.7: Electrical resistance of heater as a function of temperature

3.5.3 Porosity estimation

Since the electrochemical etching process that used for fabricating porous silicon was calibrated for refractive index, A method to estimate porosity from refractive index (or dielectric constant) is necessary. There are several models to describe dielectric property of materials that comprise two or more elements, and Bruggeman's model is one of them. The model is used to describe materials composed of two different elements. The relation between fraction and dielectric constant of each material, and dielectric constant of the effective medium is given as

$$f_a \frac{\epsilon_a - \epsilon_{eff}}{\epsilon_a + \epsilon_{eff}} + f_b \frac{\epsilon_b - \epsilon_{eff}}{\epsilon_b + \epsilon_{eff}} = 0 \tag{3.28}$$

where f_a and f_b are fraction of material a and b, and ϵ_a, ϵ_b and ϵ_{eff} are dielectric constants of material a, b and effective medium, respectively.

3.6 Results and discussion

3.6.1 Reference (SiO_2) sample

Before measuring porous silicon samples, thermally grown silicon dioxide sample was measured as a reference to confirm the experimental approach. The 1 μm SiO_2 layer was grown on intrinsic $\langle 100 \rangle$ silicon substrate. Comparison sample without SiO_2 layer was also prepared on identical substrate.

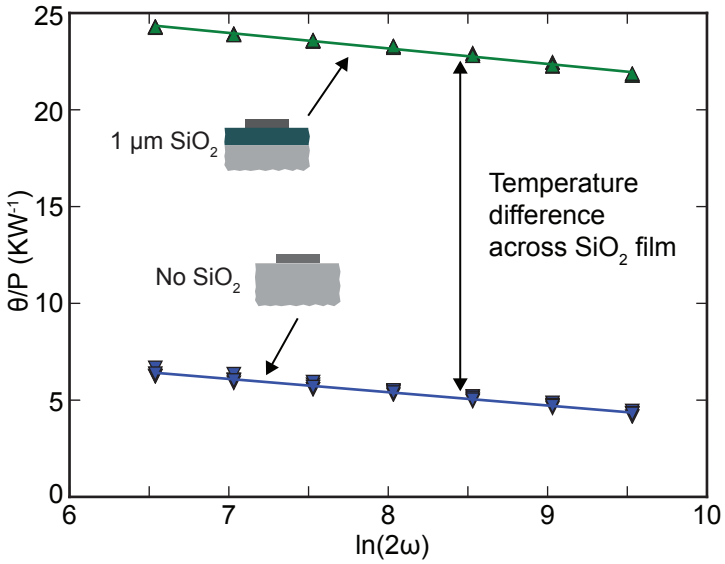

Figure 3.8: $\theta_{2\omega}/P$ as a function of $\ln 2\omega$, blue is bare intrinsic silicon and green is thermal SiO_2 on intrinsic silicon.

Figure 3.8 plots $\theta_{2\omega}/P$ of two samples as a function of $\ln(2\omega)$, which is analogous to equation 3.19. The blue dots and fitting line at bottom represent bare intrinsic

silicon, while green represent thermal SiO_2 on identical silicon substrate. Thermal conductivity of substrate was derived from each slope using equation 3.21, and the values are about 100-115 $Wm^{-1}K^{-1}$. The cross-plane thermal conductivity of SiO_2 was derived from distance between two lines using equation 3.24, and the value is 0.828 $Wm^{-1}K^{-1}$. The thermal conductivities of intrinsic silicon and SiO_2 are 150 $Wm^{-1}K^{-1}$ and 1.4 $Wm^{-1}K^{-1}$ at room temperature[[ref]], in approximate agreement with our measurement.

3.6.2 Porous silicon from moderately doped substrate

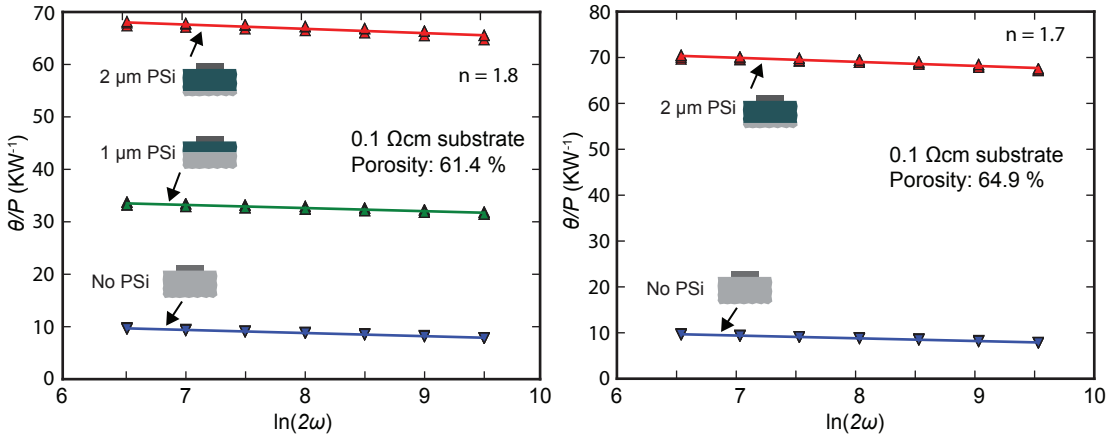

Figure 3.9: θ/P as a function of $\ln 2\omega$, blue is bare intrinsic silicon. Green and red are 1 μm and 2 μm of PSi on substrate. Top: porosity of 64.9 % Bottom: porosity of 61.4 %

Figure 3.9 shows the 3-ω measurement results of porous silicon fabricated from moderately doped substrate. A silicon wafer with resistivity of 0.1 Ω·cm was used as substrate. Porous silicon made from this substrate exhibits a typical pore diameter

of about 10 nm. Porous silicon sample with porosity of 64.9 % (fig 3.9 top) and 61.4 % (fig 3.9 bottom) were measured. Porosity was calculated from refractive index of 1.7 and 1.8 using Bruggeman's model. On both plots, blue represents substrate-only sample, green represents 1 μm psi layer on substrate and red represents 2 μm psi layer on substrate. Thermal conductivity of substrate and porous silicon was derived using equation 3.21 and 3.24. The values are shown on table below.

Table 3.2: $k_{PSi,z}$ measurement result for moderately doped porous silicon

Porosity	PSi Thickness	$k_{PSi,z}$
61.4 %	1 μm	0.63 $Wm^{-1}K^{-1}$
61.4 %	2 μm	0.57 $Wm^{-1}K^{-1}$
64.9 %	2 μm	0.47 $Wm^{-1}K^{-1}$

Measured value with moderately doped p-type porous silicon agrees with previously reported values of p or p+ type porous silicon. Prediction of thermal conductivity trend that depends on porosity is difficult from current data that only show subtle difference. However, it can be expected that thermal conductivity decreases as the porosity increases.

3.6.3 Porous silicon from highly doped substrate

Figure 3.10 shows 3-ω measurement results of porous silicon fabricated from highly doped substrate. Silicon wafer with resistivity of 1-5 mΩ·cm was used as substrate. Porous silicon made from this substrate exhibits a typical pore size of about 50 nm. Porous silicon sample with porosity of 61.4 % was measured. As above, the porosity was estimated from refractive index of 1.8 using Bruggeman's model. Blue represents substrate-only sample, green represents 1 μm psi layer on

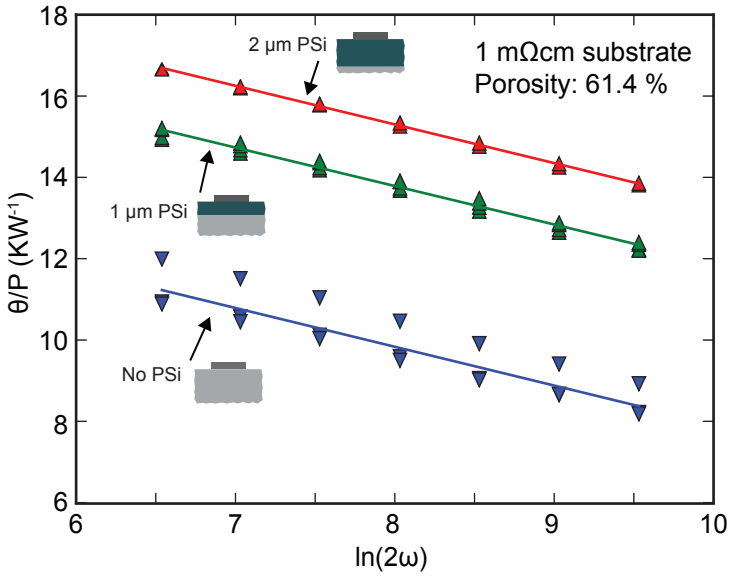

Figure 3.10: θ/P as a function of $\ln 2\omega$, blue is bare intrinsic silicon. Green and red are 1 μm and 2 μm of PSi on substrate.

substrate and red represents 2 μm psi layer on substrate. The thermal conductivity of substrate and porous silicon was derived using equation 3.21 and 3.24. The values are shown on table below.

Table 3.3: $k_{PSi,z}$ measurement result for highly doped porous silicon

Porosity	PSi Thickness	$k_{PSi,z}$
61.4 %	1 μm	3.12 $\mathrm{Wm^{-1}K^{-1}}$
61.4 %	2 μm	4.78 $\mathrm{Wm^{-1}K^{-1}}$

Highly doped porous silicon exhibits about 1 order of magnitude higher thermal conductivity compared to moderately doped porous silicon. The biggest difference between two porous silicon samples is pore size. Porous silicon with larger pore diameter features relatively bigger leftover silicon skeleton compared to those with smaller pores. It is clear that nanoscale feature size of material contributes more on

its thermal property than porosity.

3.7 Summary

In this chapter, the theory and experimental details of 3-ω thermal conductivity measurement was introdued and applied to study the thermal conductivity of prous silicon. The 3-ω method provides a relatively simple and accurate way to measure the thermal conductivity of bulk and thin film materials. Moderately doped porous silicon shows similar thermal conductivity value of p or p+ type porous silicon that has been reported previously. Highly doped porous silicon has thermal conductivity of one order of magnitude larger than moderately doped porous silicon. The result shows that nanoscale feature size plays an important role on material's thermal property

Chapter 4: Strong anisotropic thermal conductivity of porous silicon

In previous chapter, porous silicon thin film's cross-plane thermal conductivity was measured by differential 3-ω method. For isotropic materials, it can be safely assumed that the measured cross-plane thermal conductivity is identical to the in-plane component. However anisotropic materials exhibit different thermal conductivities along the different axes, and therefore requires separate measurements to accurately characterize both components. All previous studies that reported porous silicon's thermal conductivity assumed that porous silicon is a thermally isotropic material. However porous silicon is expected to exhibit anisotropy in thermal conductivity based on its strongly directional nanoscale structure. Figure 1.1 in chapter 1 shows a scanning electron micrograph of porous silicon that has strong columnar pore structure. Such an anisotropic structure strongly suggest that porous silicon will have unique anisotropic physical properties, including thermal conductivity. The in-plane thermal conductivity is particularly important for thermal sensors such as bolometers or micro-heaters [30, 31, 52, 53]. Those devices usually employ suspended thin film structure for thermal isolation to maximize its performance. In-plane thermal conductivity dominates heat transfer in such devices and also governs the cross-talk between neighboring pixels in bolometric imaging system. Direct

measurement of thin film's in-plane thermal conductivity often involves fabricating sample with suspended structure or encapsulating the film between insulation layers [54, 55]. However, preparing porous silicon samples for those methods with additional heating and sensing structure is extremely challenging process. A recently developed non-contact method called the transient thermal grating does not require any heater, sensor or transducer structure, however requires extensive analysis to avoid error and possibility of laser induced oxidation [56]. While direct measurement methods are challenging, the 3-ω method provide alternative way to measure in-plane thermal conductivity with identical sample fabrication process to cross-plane measurement. In the differential 3-ω measurement, sample is prepared with wide heater compared to film thickness, in order to minimize the heat spreading into the film ($b \gg d$). In this limit, the heat diffusion process depends only on cross-plane thermal conductivity. If heater width is comparable or smaller than film thickness ($b \approx d$ or $b \ll d$), a significant portion of heat will spread into the film instead of diffusing into substrate. In this case, heat diffusion depends on both cross-plane and in-plane components, and resulting temperature oscillation amplitude will be reduced compared to the case of no heat spreading. Borca-Tasciuc *et al.* analyzed the effect of such heat spreading inside film on substrate geometry and derived analytical expression, which includes argument of in-plane thermal conductivity of film, for correct cross-plane thermal conductivity from differential 3-ω measurement [57]. This method provides a good way to indirectly estimate in-plane thermal conductivity of thin film without resorting to difficult fabrication process.

Another indirect approach to characterize the in-plane thermal conductivity

is using numerical simulation that precisely describes actual 3-ω experiment and compare the result to experimental measurement. If simulation is performed with the correct amount of in-plane thermal conductivity, the numerically computed temperature oscillation should match with experimental result.

In this chapter, experimental and analysis method of measuring in-plane thermal conductivity of porous silicon by differential 3-ω method will be described. Later, numerical simulation method will be discussed and the result will be compared with experimental result.

4.1 2D heat flow model

4.1.1 Multilayer film on substrate

Original 3-ω and differential 3-ω analysis method described in the previous chapter do not account for 2-dimensional heat diffusion inside film. Chen *et al.* [58] derived solution for heater temperature rise of anisotropic film on semi-infinite substrate, and Kim *et al.* [59] derived solution for heater temperature rise of multilayer isotropic film on substrate. Later, Borca-Tasciuc *et al.* [57] derived general solution for 2-dimensional heat conduction based on those two studies. The general 2D solution is able to analyze temperature rise of metal heater on anisotropic multilayer film on substrate. The structure is shown on figure 4.1. The temperature rise (amplitude of temperature oscillation) is expressed as

$$\theta = \frac{-P}{\pi L k_{z1}} \int_0^\infty \frac{1}{A_1 B_1} \frac{\sin^2(b\lambda)}{b^2\lambda^2} d\lambda \tag{4.1}$$

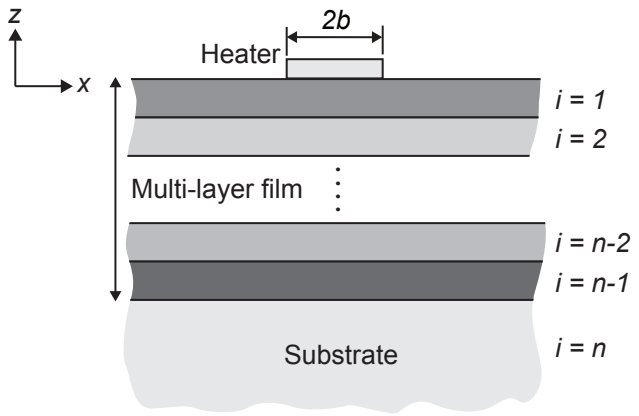

Figure 4.1: Multilayer film on substrate 2D heat flow model

where

$$A_{i-1} = \frac{A_i \frac{k_{i,z}B_i}{k_{i-1,z}B_{i-1}} - \tanh(\phi_{i-1})}{1 - A_i \frac{k_{i,z}B_i}{k_{i-1,z}B_{i-1}} \tanh(\phi_{i-1})}, i = 2, 3...n \tag{4.2}$$

$$B_i = (k_{i,xz}\lambda^2 + \frac{i2\omega}{D_{i,z}})^{1/2} \tag{4.3}$$

$$\phi_i = B_i d_i, k_{xz} = k_x/k_z \tag{4.4}$$

n is the total number of layers, subscript x and z correspond to the directions parallel and perpendicular to film surface respectively. $i = n$ for substrate and $A_n = -1$ if substrate is semi-infinite.

4.1.2 Single anisotropic film on isotropic substrate

A porous silicon film on crystalline silicon substrate can be described by a single, anisotropic layer, on an isotropic substrate. Under AC heating, the temperature rise in this case is expressed as,

$$\theta_{F+S} = \frac{-P}{\pi L k_{F,z}} \int_0^\infty \frac{1}{A_F B_F} \frac{\sin^2(b\lambda)}{b^2\lambda^2} d\lambda \tag{4.5}$$

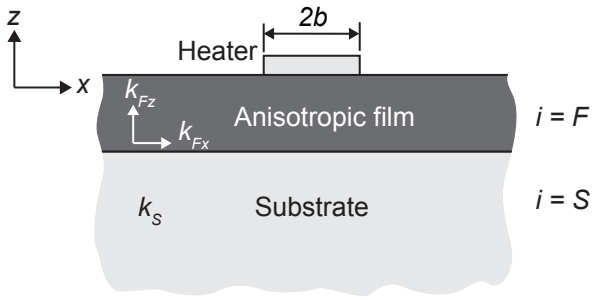

Figure 4.2: Anisotropic film on substrate

where

$$A_F = \frac{A_S \frac{k_S B_S}{k_{F,z} B_F} - \tanh(\phi_F)}{1 - A_S \frac{k_S B_S}{k_{F,z} B_F} \tanh(\phi_F)} \tag{4.6}$$

$$B_F = (k_{F,xz}\lambda^2 + \frac{i2\omega}{D_{F,z}})^{1/2} \tag{4.7}$$

$$\phi_F = B_F d_F, k_{F,xz} = k_{F,x}/k_{F,z} \tag{4.8}$$

where subscript F and S means film and substrate respectively. Similarly, the temperature rise when the film is absent given by

$$\theta_S = \frac{-P}{\pi L k_{F,z}} \int_0^\infty \frac{1}{A_S B_S} \frac{\sin^2(b\lambda)}{b^2\lambda^2} d\lambda \tag{4.9}$$

where

$$A_S = -1 \tag{4.10}$$

$$B_S = (\lambda^2 + \frac{i2\omega}{D_S})^{1/2} \tag{4.11}$$

From the above general expression, factors that affect simple 1D heat flow approximation can be derived [57]

$$\Delta T_F = T_{F+S} - T_S = \frac{Pd}{2bLk_{F,z}} CS \tag{4.12}$$

where C is a dimensionless "contrast factor" given by

$$C = 1 - \frac{k_{F,x}k_{F,z}}{k_S^2} \tag{4.13}$$

and S is a dimensionless "spreading factor" that is found to be

$$S = \frac{2}{\pi}\int_0^\infty \frac{\sin^2\lambda}{\lambda^3}\frac{\tanh(\lambda\beta_F)}{[1+(\sqrt{k_{F,z}k_{F,x}}/k_S)\tanh(\lambda\beta_F)]\beta_F} \tag{4.14}$$

The ratio of true cross-plane thermal conductivity (k_F, z) to measured value with 1D approximation (k_{1D}) is expressed as

$$\frac{k_F, z}{k_{1D}} = CS \tag{4.15}$$

If film and substrate thermal conductivity contrast is large enough, then $C \approx 1$. In this case, the expression can be simplified as

$$k_{F,z} = k_{1D} \times F(\beta_F) \tag{4.16}$$

where

$$F(\beta_F) = \frac{2}{\pi}\int_0^\infty \frac{\sin^2 x}{x^3}\frac{\tanh(x\beta_F)}{\beta_F}dx \tag{4.17}$$

and

$$\beta_F = \sqrt{\frac{k_{F,x}}{k_{F,z}}}\left(\frac{d}{b}\right) \tag{4.18}$$

Note that in case of small β_F (either $k_{F,x} \ll k_{F,z}$ or $b \gg d$), $F(\beta_F)$ approaches to 1, which means the Equation 4.16approaches to Equation 3.24 which is valid for 1D heat flow regime. The ratio $F(\beta_F)$ is shown in figure 4.3 as a function of β_F. On this plot, the heat flows is approximately 1-dimensional for $\beta_F < 10^{-1}$, while amount of heat spreading quickly increase as β_F increases.

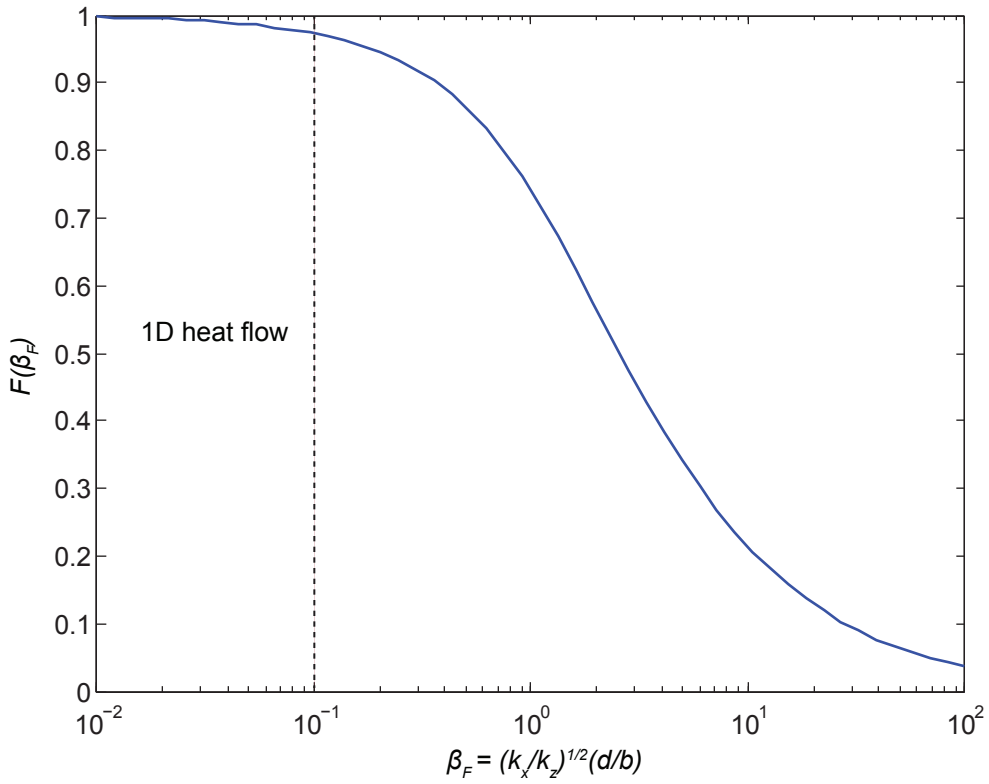

Figure 4.3: $F(\beta_F)$ as a function of β_F

A sample with geometry that allows more in-plane directional heat flow provides more precise estimate of $k_{F,x}$. This means high aspect ratio of d/b is desirable. Dames calculated sensitivity to $k_{F,z}$ and $k_{F,x}$ as a function of "dimensionless heater width", which is reciprocal of β_F, and suggested a range smaller than 0.1 ($\beta_F > 10$) for accurate measurement [29]. However, this imposes a constraint on the sample geometry. The thermal wavelength or thermal penetration depth is expressed as

$$\lambda_t = \sqrt{\frac{D}{2\omega}} \tag{4.19}$$

while D is thermal diffusivity and ω is electrical frequency of driving current. Since λ_t should be in range $d \ll \lambda_t \ll d_{sub}$ to avoid abnormal response due to film-substrate and substrate-environment interfaces, the film thickness need to be kept rather small in order not to limit driving frequency range. Also, patterning metal strip narrower than 1-2 μm requires higher-resolution nanolithographic processing, such as electron-beam lithography. To satisfy these constraints with a 500 μm thick silicon substrate and 40 μm thick porous silicon film would limit the frequency to a range well within 30 Hz - 4000 Hz. Assuming narrowest heater width that can be fabricated is 4 μm, the suggested regime, $\beta_F > 10$, can only be satisfied with near isotropic thermal conductivity which does not apply for porous silicon.

The constraints are able to be overcome by measuring multiple samples that have various combination of b and d. It is possible to estimate $k_{F,x}$ by measuring two samples, one with dimension of $b \gg d$ and the other with dimension $b \ll d$ or $b \approx d$, and applying the Equation 4.16 to the result to find $k_{F,x}$ that makes $k_{F,z}$ from two samples same value. However, multiple samples with varying geometry allow

more accurate measurement by providing a series of data with certain trend as a function of sample geometry, instead of single data which may contain significant error. If correct $k_{F,x}$ value is used for calculation, The predicted $k_{F,z}$values obtained all experimental samples would be self consistent and would match to true $k_{F,z}$ value.

4.1.3 Sample Fabrication

The fabrication process of samples for in-plane measurement is similar to the cross-plane measurement described in the previous chapter. Porous silicon samples were fabricated from p-type (1-5 m$\Omega\cdot$ cm) $\langle 100 \rangle$ silicon wafer. All samples has porosity of 59 % (estimated from refractive index 1.85) In this measurement, a series of samples with several different combinations of b and d, as well as substrate only ($d = 0$) samples with various b, were prepared. Figure 4.4 illustrates cross section of two samples at both end of aspect ratio. Sample on left side shows geometry of large b and small d (aspect ratio $b/d \approx 5$). Differential 3-ω measurement result performed on this sample can be interpreted as $k_{F,z}$ within 5 % error based on the geometry (with isotropic assumption). The sample shown on right side has geometry of small b and large d (aspect ratio $b/d \approx 0.05$), which is much more sensitive to $k_{F,x}$. Table 4.1 lists all combinations of b and d that were measured. Each devices resistance and dR/dT were characterized using standard four-probe measurement technique. The dR/dT measurement results of the samples with 6 different heater width are shown on figure 4.5 Total of 30 devices were prepared with combination of different heater widths (4, 10, 16, 22, 28, 34 μm) and porous silicon thicknesses

(5, 15, 25, 35 μm and no PSi).

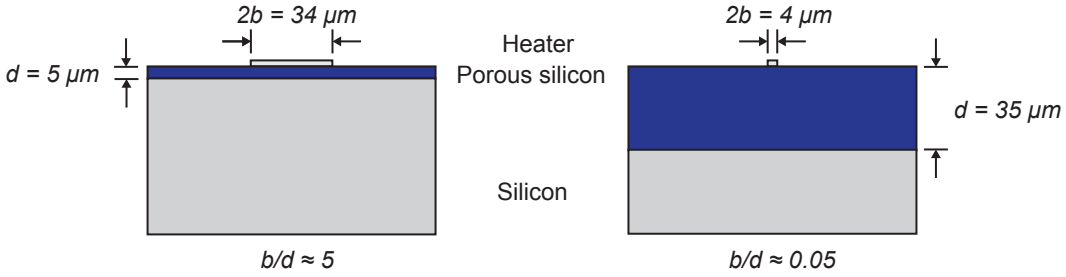

Figure 4.4: Prepared sample with highest b/d (left) and lowest b/d (right).

4.1.4 Experimental result and discussion

The instrumentation, measurement and data analysis methods are identical to the differential 3-ω method described in previous chapter. $V_{3\omega}$ for all prepared devices were measured within driving frequency (ω) range between 50 and 1000 Hz. Measured $V_{3\omega}$ values were converted to θ/P with equation 3.11. Results are plotted on figures **??**. On each figure, θ/P of devices of same heater width ($2b$) are compared.

First, substrate-only samples with various b are compared on figure 4.6. Theoretically, temperature rise of these samples supposed to be identical. On actual experiment, overall temperature slightly increase as b decrease. This difference results from thin SiO_2 electrical insulation layer which added resistance between heater and silicon substrate. This is not an issue because $\Delta\theta/P$ is only compared between samples of same b. Also, difference in temperature rise is relatively minor compared to temperature rise of porous silicon samples. Substrate thermal conductivity

Table 4.1: List of samples with different PSi thickness (d) and heater width ($2b$).

Sample (Number)	PSi thickness (μm)	Width (μm)	Resistance (Ω)	dR/dT (Ω/K)
1	No PSi	2.8	430	0.527
2	No PSi	9.1	143	0.173
3	No PSi	15.2	85.9	0.102
4	No PSi	21.5	60.3	0.0761
5	No PSi	28	47.1	0.0575
6	No PSi	33.5	38.9	0.0459
7	5	4.2	305	0.386
8	5	10.4	125	0.149
9	5	16.8	78.4	0.094
10	5	22.7	57.3	0.0715
11	5	29.2	44.7	0.0549
12	5	35.3	37	0.043
13	15	4	329	0.403
14	15	10.5	130	0.148
15	15	16.7	80.3	0.0945
16	15	22.2	61.5	0.0731
17	15	28.3	47.9	0.0569
18	15	34.6	39	0.0443
25	35	4.6	287	0.356
26	35	10.7	124	0.145
27	35	16.7	79.4	0.0945
28	35	22.3	60.6	0.0727
29	35	28.3	47.3	0.0569
30	35	34.5	39.2	0.0444

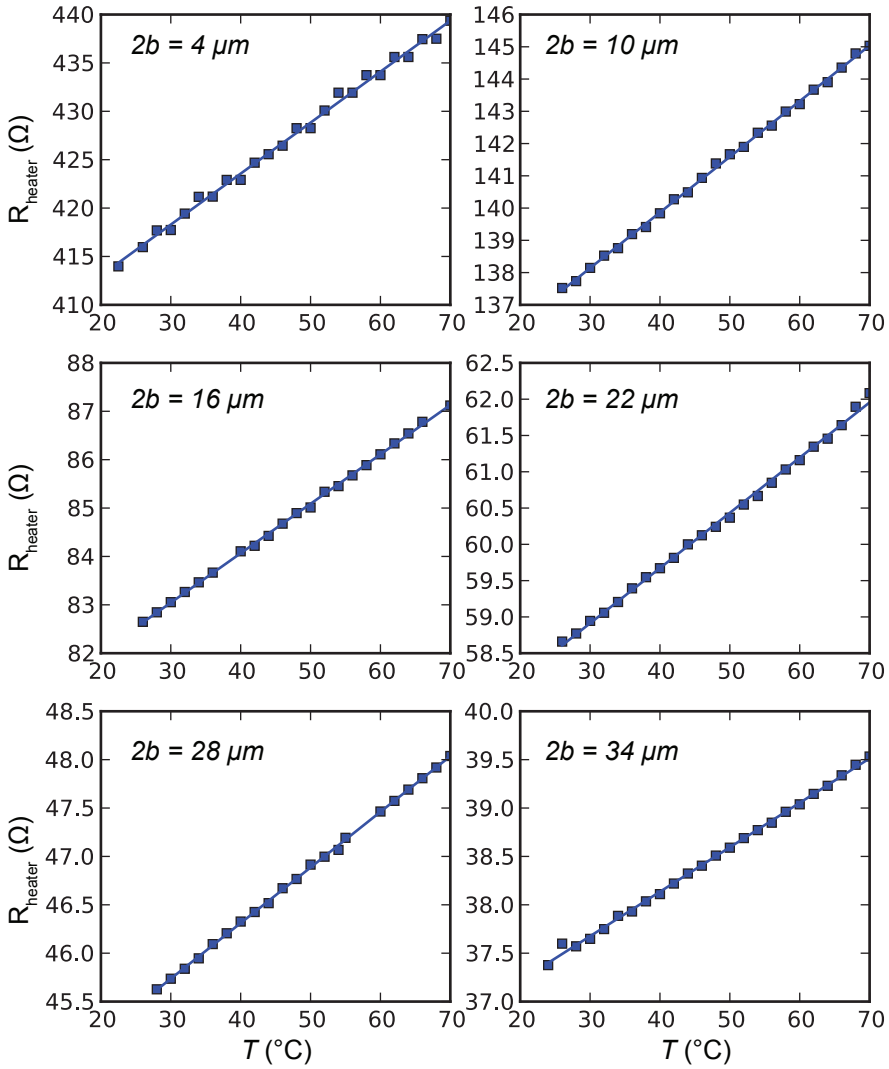

Figure 4.5: The heater resistance vs. temperature of samples with 6 different heater width

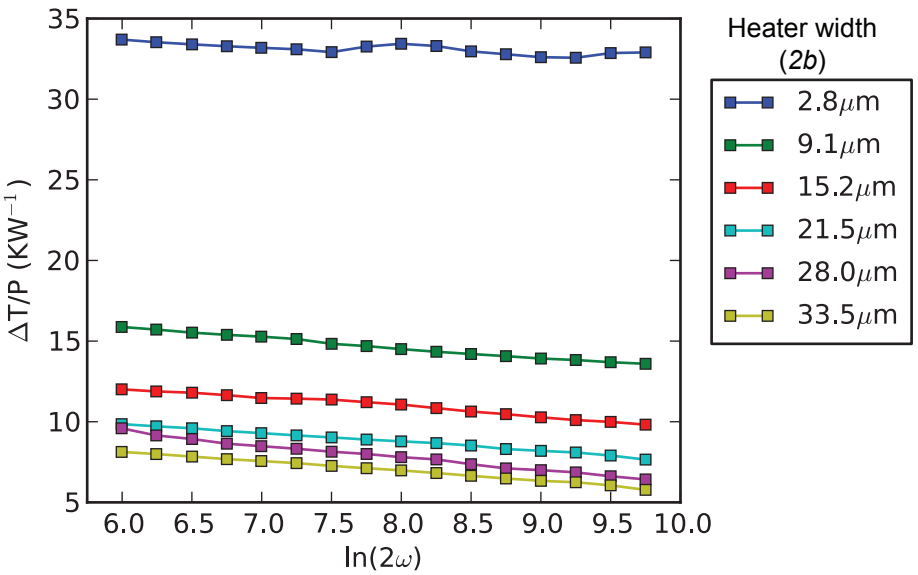

Figure 4.6: Results of reference samples (samples 1 - 6). Numbers in legend represent heater widths.

value,k_{Sub}, derived form slope was about 130 $\mathrm{Wm^{-1}K^{-1}}$.

Figure 4.7, 4.8, 4.9, 4.10, 4.11 and 4.12 shows comparison of temperature rise between samples of same b with different PSi thickness. Note that devices on 25μm thick PSi layer were over exposed during fabrication process, ended up with about one step wider heater width (10 - 38 mum instead of 4 - 34 μm). Therefore 25 μm thick PSi data is missing on figure 4.7. It is observed for all b that amount of temperature rise ($\Delta\theta/P$) increase quite linearly as PSi thickness increase up to 25 μm. However, increase rate clearly diminished between 25 and 35 μm. This observation agrees with 2D heat flow model; increased d cause more heat flow into film and reduce temperature rise of heater.

$k_{PSi,z}$ of each sample was derived from $\Delta\theta/P$ with equation3.24. Results are on Table 4.2. Also the values are plotted as a function of b/d

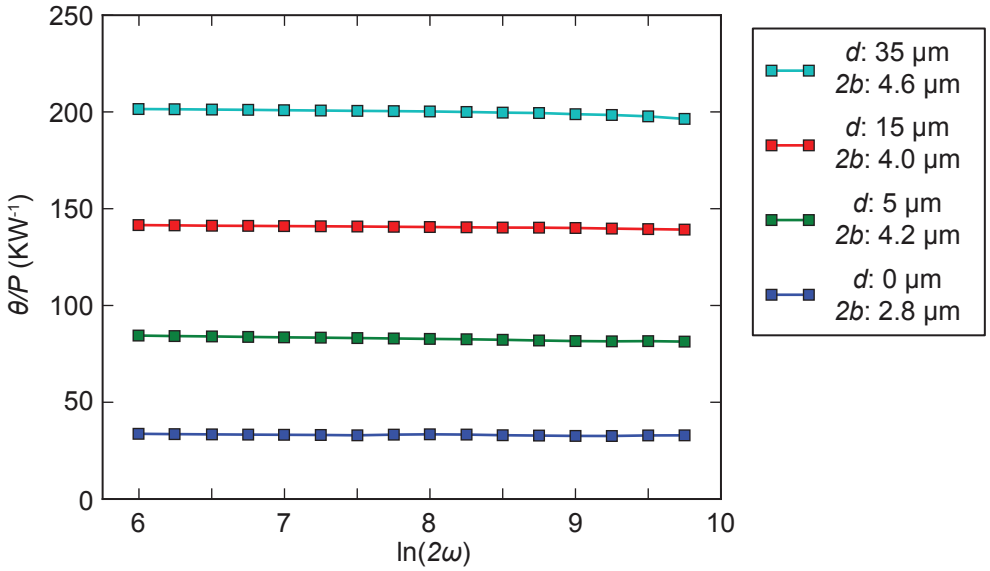

Figure 4.7: Samples 1, 7, 13, 25. Heaters' nominal width is 4 μm. '$d = 0$ μm' represents no-PSi sample (reference).

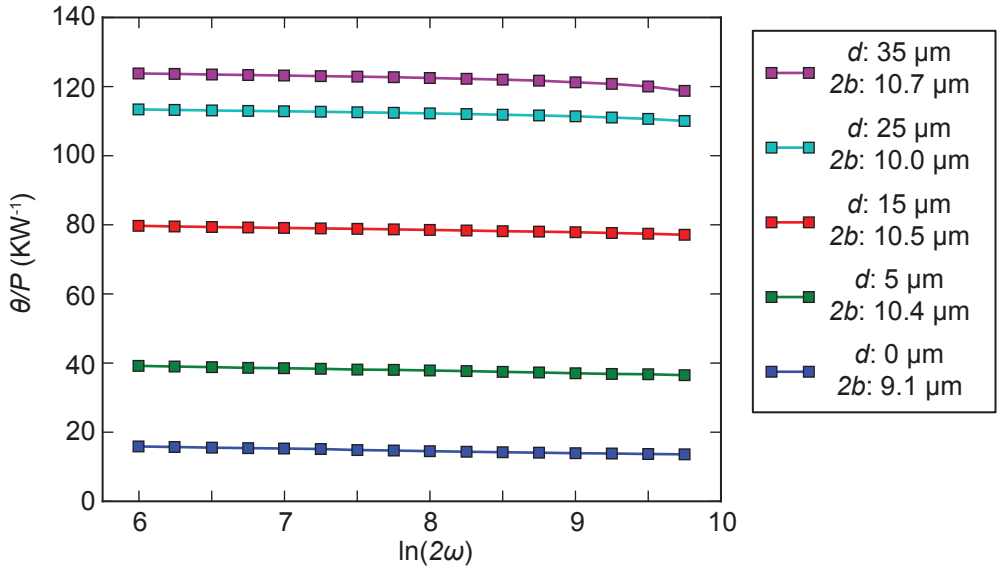

Figure 4.8: Samples 2, 8, 14, 19, 26. Heaters' nominal width is 10 μm. '$d = 0$ μm' represents no-PSi sample (reference).

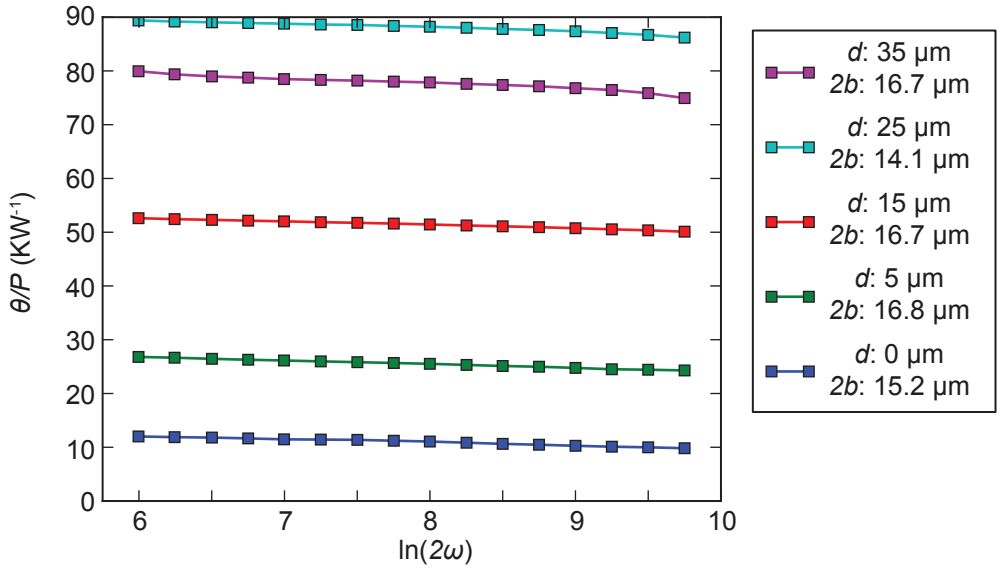

Figure 4.9: Samples 3, 9, 15, 20, 27. Heaters' nominal width is 16 μm. '$d = 0$ μm' represents no-PSi sample (reference).

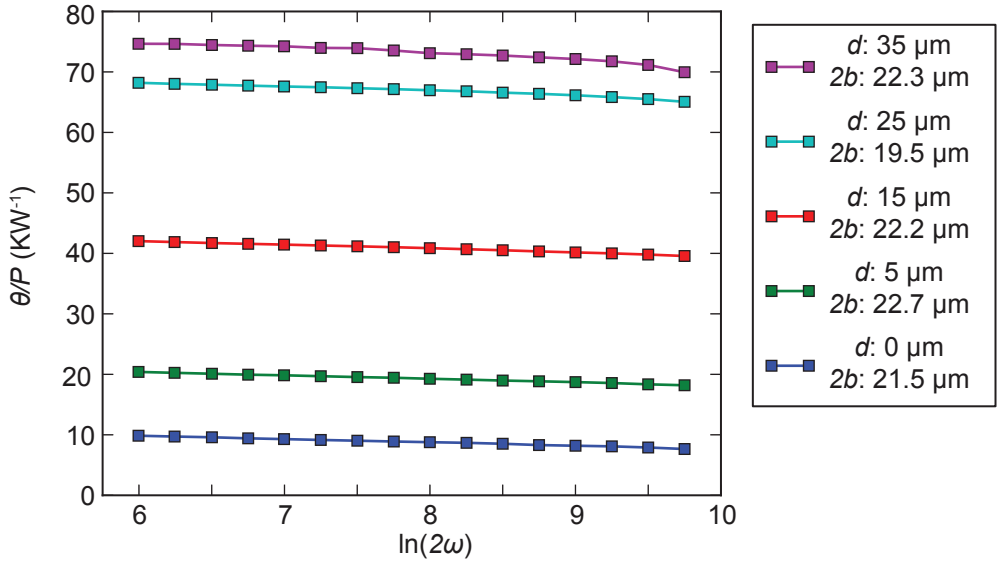

Figure 4.10: Samples 4, 10, 16, 21, 28. Heaters' nominal width is 22 μm. '$d = 0$ μm' represents no-PSi sample (reference).

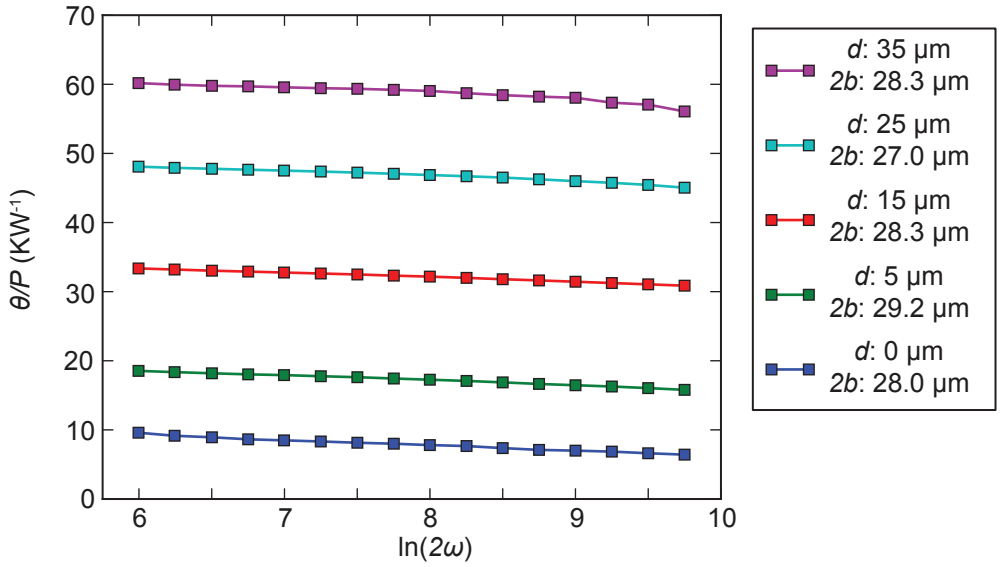

Figure 4.11: Samples 5, 11, 17, 22, 29. Heaters' nominal width is 28 μm. '$d = 0$ μm' represents no-PSi sample (reference).

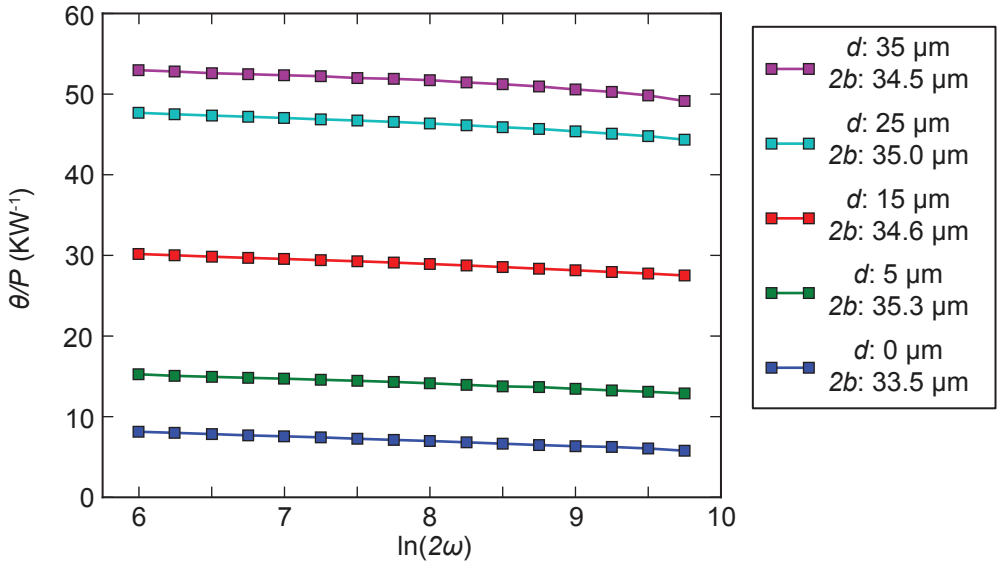

Figure 4.12: Samples 6, 12, 18, 23, 30. Heaters' nominal width is 34 μm. '$d = 0$ μm' represents no-PSi sample (reference).

Table 4.2: Sample dimensions and thermal conductivities ($k_{PSi,z}$) estimated by 1D assumption.

Sample (Number)	Heater width ($2b$) (μm)	PSi thickness (d) (μm)	$k_{PSi,z}$ ($\mathrm{Wm^{-1}K^{-1}}$)
7	4.2	5	11.9
8	10.4	5	10.3
9	16.8	5	10.2
10	22.7	5	10.4
11	29.2	5	9.11
12	35.3	5	9.94
13	4	15	17.4
14	10.5	15	11.1
15	16.7	15	11.1
16	22.2	15	10.5
17	28.3	15	10.9
18	34.6	15	9.89
19	10	25	12.8
20	14.1	25	11.4
21	19.5	25	11.0
22	27	25	11.8
23	35	25	9.09
25	4.6	35	22.8
26	10.7	35	15.2
27	16.7	35	15.6
28	22.3	35	12.2
29	28.3	35	12.1
30	34.5	35	11.3

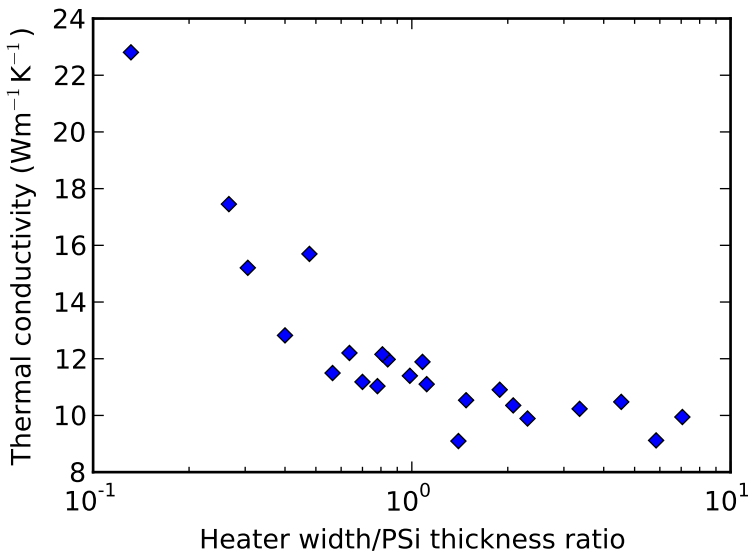

Figure 4.13: Estimated thermal conductivity with 1D assumption as a function of "heater width/PSi thickness" ratio

Since these results are derived using 1D heat flow approximation, the values only valid when $b \gg d$ satisfied. On figure 4.13, k_{1D} approaches to about 10 $\mathrm{Wm^{-1}K^{-1}}$ as b/d ratio increases. This right side of plot is close to typical differential 3-ω measurement regime where $b \gg d$. Therefore $k_{PSi,z}$ can be assumed to be about 10 $\mathrm{Wm^{-1}K^{-1}}$. As b/d decreases k_{1D} gradually increases. This result caused by reduced $\delta\theta/P$ in the regime $b < d$ or $b \approx d$. These values were corrected by 2D heat flow model with proper in-plane thermal conductivity value, $k_{PSi,x}$. If correct $k_{PSi,x}$ is used for correction, all values on plot should be same as the value at $b \gg d$ regime.

Figure 4.14 shows estimated $k_{PSi,z}$ by equation4.16 with three different assumptions. When 1D heat flow is assumed ($k_{PSi,x} \approx 0$), estimated $k_{PSi,z}$ values are identical to differential measurement because $F(\beta_F)$ approaches 1. If $k_{PSi,x} = k_{PSi,z}$

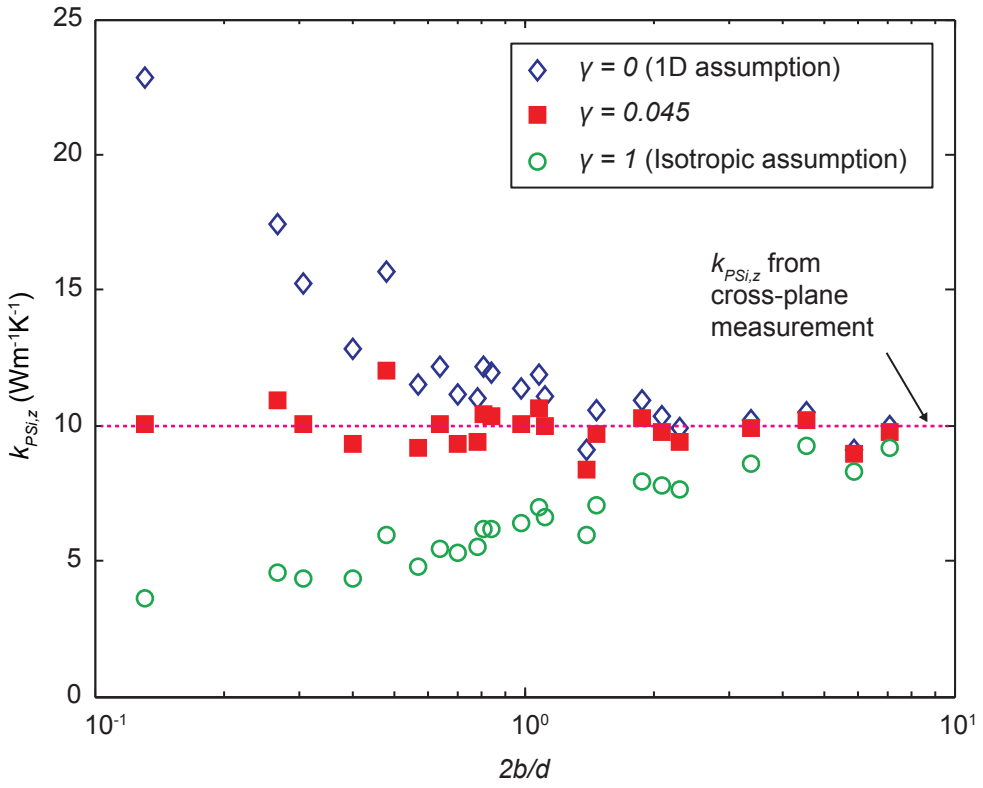

Figure 4.14: Estimated $k_{PSi,z}$ with $k_{PSi,x} \approx 0$, $k_{PSi,x} = 0.45$ Wm^{-1}K^{-1} and $k_{PSi,x} = k_{PSi,z}$ assumptions

(isotropic assumption), estimated $k_{PSi,z}$ decreases as b/d decreases, which shows opposite trend compared to the 1D assumption. The trend gets close to flat at around 10 Wm^{-1}K^{-1} when $k_{PSi,x} = 0.45$ Wm^{-1}K^{-1}; this is in-plane thermal conductivity of PSi derived with 2D heat flow analysis method. Compared to cross-plane thermal conductivity of 10 Wm^{-1}K^{-1}, in-plane component is greatly reduced by factor of 20.

4.2 Numerical simulation with comparable experiment

Another way to indirectly infer in-plane thermal conductivity is using numerical simulation. By modeling actual 3-ω samples with correct dimensions and thermal properties and applying sinusoidal heat flow, θ of the model was calculated. The simulation result with various in-plane thermal conductivity values is compared to experimental result, then actual in-plane component value was inferred by matching simulation and experimental result. Compared to analytical approach mentioned above, using numerical simulation does not require specific regime in samples geometry thus eliminates difficulty of fabricating samples with challenging geometry. Also, experiment becomes more convenient since it does not need differential measurement between actual sample and reference sample.

Experimental measurement with parameters that carefully matched with simulation was carried out using same set of samples of previous section.

4.2.1 Simulation

We used CST Multiphysics Studio's thermal transient solver to numerically calculate temperature oscillation of samples. The software calculates temporal temperature variation of defined model by means of finite-element time-domain method. The model defined for simulation is illustrated in figure 4.15.

Half of sample cross section with finite thickness was modeled for fast calculation. Appropriate boundary conditions were applied on each surface of computation box to properly account for entire sample. Thermal conductivity of silicon

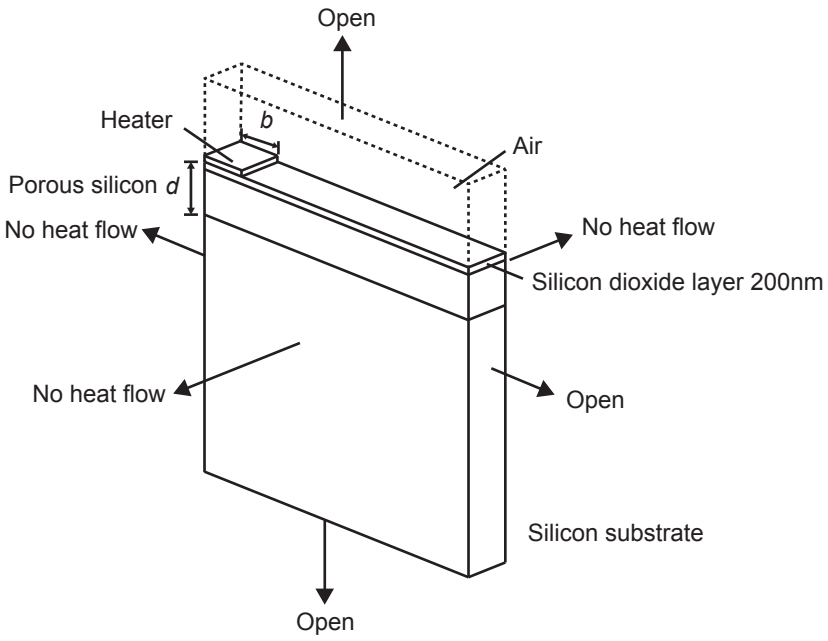

Figure 4.15: Schematic diagram of the numerical simulation model

substrate and cross-plane thermal conductivity of porous silicon derived from previous section were used as parameters. Another necessary parameter for simulation is heat capacity of porous silicon. Since porous silicon is simply crystalline silicon that partial volume is substituted with air, it is reasonable to approximate the value as $C_{PSi} = C_{Si} \times (1 - \text{porosity})$, where C_{PSi} and C_{Si} are heat capacity of porous silicon and silicon substrate. To assume in-plane component of porous silicons thermal conductivity, we introduced anisotropy factor γ, which represents $k_{PSi,x}/k_{PSi,z}$. The solver calculates temperature gradient of the model at each small time step while sinusoidal heat flow is excited at heater surface. Heat flow density from heater surface kept constant at 1×10^5 Wm^{-2} regardless of dimension. Temperature at the center of heater is monitored and then converted to amplitude of temperature oscillation θ, to be compared with experimental data. The simulation was run multiple times

with varying b, d and γ to get entire solution of θ as a function of b for several different porous silicon thickness and γ. A simulation without porous silicon layer was performed separately to be compared with reference experimental sample.

4.2.2 Experiment

The same set of samples from previous section was used. Instrumentation was also identical. In this experiment, $V_{3\omega}$ was measured at single frequency that matches with simulation ($\omega/2\pi$ = 500 Hz). Driving current to generate 1×10^5 Wm^{-2} was calculated prior to experiment and carefully adjusted. Measured $V_{3\omega}$ was converted to θ with equation 3.11.

4.2.3 Result and discussion

Simulation results and experimental data are compared in figure 4.17 by plotting θ as a function of b. Note that it is possible to plot θ as a function of d for same analysis. However keeping d consistent in actual fabrication process is more reliable than keeping b consistent. Before testing actual samples, reference sample that does not have porous silicon layer was tested and compared to corresponding simulation model. This step is important to ensure that our simulation model agrees well with real sample and experiment. Experimental data and simulation result are compared on figure 4.17 (a). Even though there is a little deviation between experimental data and simulation result, they are very close and overall trend fits very well with each other. Figure 4.17 (b)-(d) shows comparisons between simulation results and

experimental data for porous silicon thickness of 5, 15 and 35 μm. For all cases, simulation results clearly show that θ rises as γ decreases for given geometry.

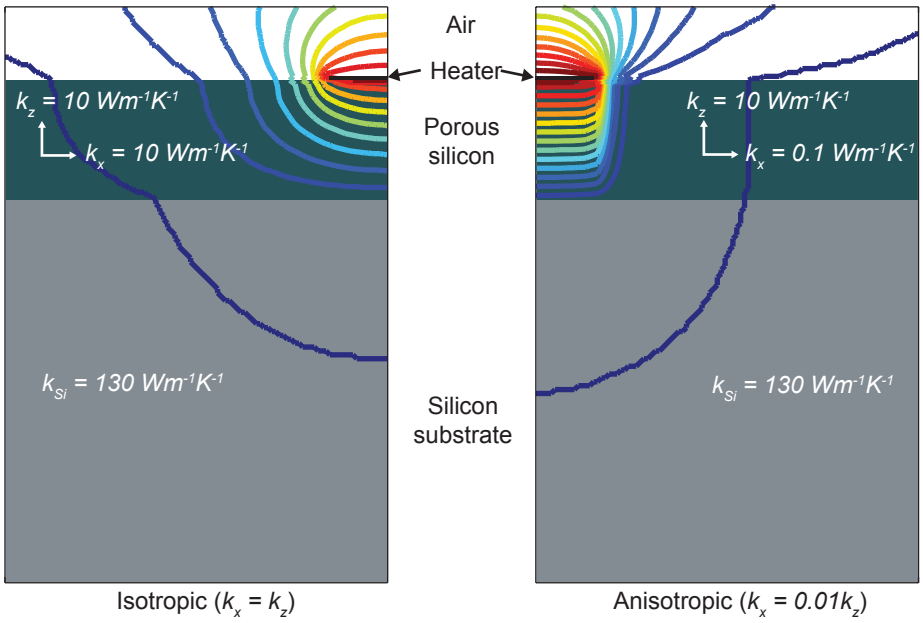

Figure 4.16: Comparison of heat spreading inside sample between isotropic and anisotropic case by numerical simulation.

On figure 4.16, difference of heater temperature rise from simulation result is visualized. Each pane visualize maximum heater temperature with $\gamma = 1$ (left) and $\gamma = 0.01$ (right). Since smaller means less heat spread inside porous silicon layer, heat flux is concentrated close to heater and raise heater temperature higher than larger γ case. Overall, experimental data (black square dots) located well above the isotropic ($\gamma = 1$) simulation results, which indicates lower in-plane thermal conductivity compared to cross-plane thermal conductivity as we predicted based on microscopic structure. For 5 μm thick case (figure 4.17 (b)), experimental data lay close to simulation results with $\gamma = 0.1$ and 0.01. However it is difficult to

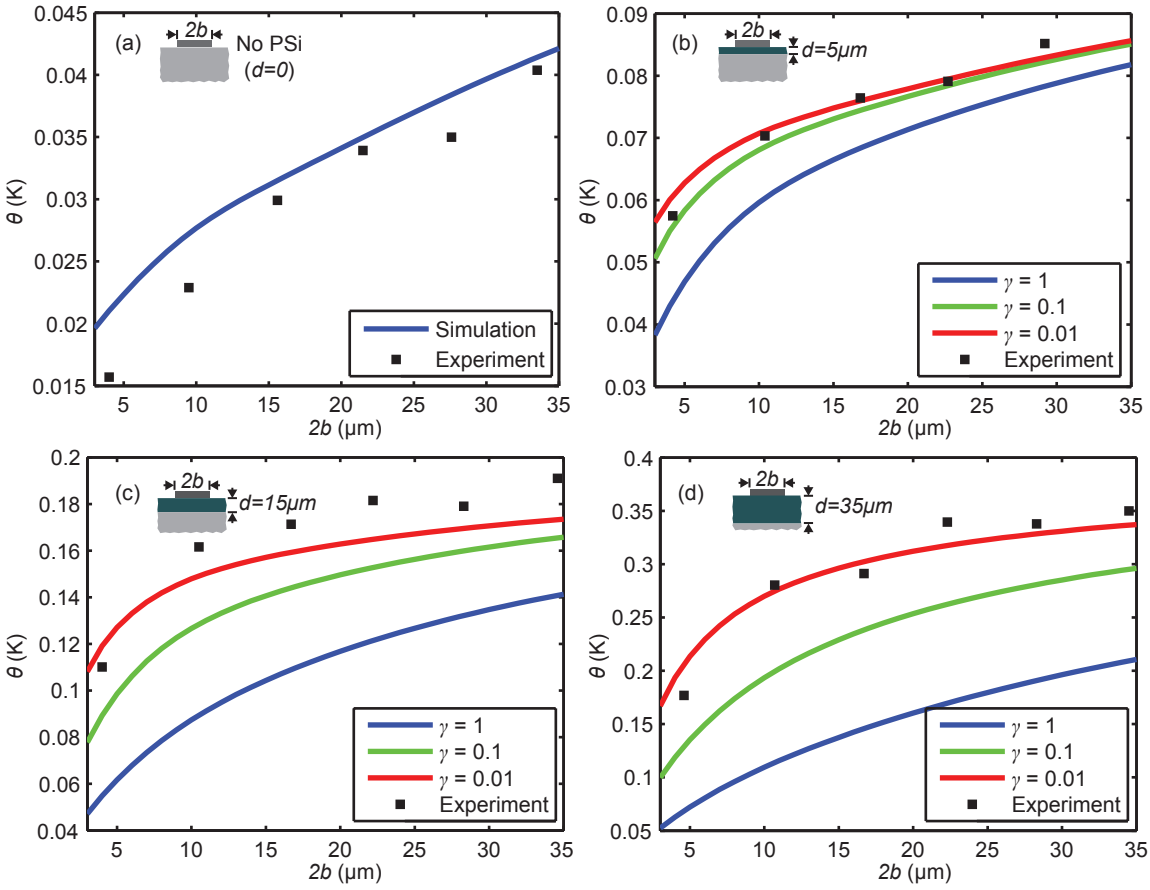

Figure 4.17: Comparison between experimental data and numerical simulation.

tell the actual fitting because spacing between those two results is too close to tell difference. This is a limitation of sample geometry with $d = 5$ μm; in most of b range falls in $b > d$ regime where cross-plane component is dominant. 15 μm thick case (figure 4.17 (c)) is in transition regime from $b > d$ to $b < d$. Experimental data lay slightly above $\gamma = 0.01$ and simulation plots are separated farther apart compared to (b). Figure 4.17 (d) describes d = 35 μm case. All simulation results are clearly separated and experimental data lined up very well with $\gamma = 0.01$ simulation. The result may not be enough to conclude exact number of in-plane thermal conductivity; however it is almost clear that in-plane component is about two orders of magnitude smaller than cross-plane component

4.3 Summary

The anisotropy of porous silicon's thermal conductivity was measured by both the 2D heat flow analysis and numerical simulation method. Both method allows to estimate in-plane thermal conductivity of the porous silicon without challenging sample fabrication process. Although the most samples were not ideal because of geometrical constraints, We were able to estimate ($k_{PSi,x}$) by 2D analysis from data obtained from a series of samples with varying geometry. Numerical simulation result supported the experimental result by 2D analysis. The result confirmed that the in-plane thermal conductivity ($k_{PSi,x}$) of porous silicon is smaller than the cross-plane conductivity ($k_{PSi,z}$) by factor of 20 to 100. More accurate measurement would require sub-micrometer scale heater to achieve smaller dimensionless heater width.

Note that samples used for this study feature pore diameter of 20 50 nm. Porous silicon's pore size and microscopic structure can greatly vary depending on substrate type and etching process. That means degree of anisotropy might be quite different for different type of porous silicon.

Chapter 5: Conclusion

5.1 Summary

Porous silicon is a versatile material that has many interesting applications. This thesis focused on porous silicon's optical and thermal properties and demonstrated possibilities as a highly sensitive optical sensor and excellent thermal insulation material.

Optical waveguide comprises nanoporous material has unique advantage for sensing application because it allows test substance to infiltrated into the core of waveguide so that optical mode and the substance interact more effectively compared to solid core waveguide sensor that only weak evanescent mode interacts with test substance. We used a process of electrochemical etching and laser oxidation to produce channel waveguides and integrated on-chip Mach-Zehnder structures, and we measured the responsivity by selectively applying isopropanol to a small waveguide segment in one arm of the interferometer. Sensitivity analysis revealed that our device surpass previously reported devices in sensitivity. Compared to previously reported porous sensors that light travels perpendicular to thin porous layer, our device employed waveguide structure that confines light in direction parallel to porous layer. Waveguide geometry enabled more sensitive detection by increasing

interaction length. By integrating MZI structure on a single chip, much better signal stability than fiber-based MZI was achieved.

Porous silicon has thermal conductivity much lower than crystalline silicon. Its thermal conductivity can be tailored by fabrication process. Porous silicon's thermal conductivity was measured with 3-ω method. The measurement system utilizes a single metal strip deposited on top of measurement sample, which serve as both a heater and a temperature sensor. At first, cross-plane thermal conductivity was measured with 1D heat flow assumption. The result was comparable to previously reported values. Porous silicon exhibits strong anisotropy in thermal conductivity. In addition to cross-plane measurement, in-plane measurement was performed with both 2D heat flow analysis and numerical simulation. The result revealed that in-plane thermal conductivity is 1-2 order of magnitude of smaller than cross-plane value.

5.2 Future work

5.2.1 Thermo-optic modulator

Another interesting aspect of porous silicon that may open to opportunity of new applications is thermo optic property. One of the applications is thermo optic modulator. The ability to make various compact and integrated optical components with matured, low cost silicon fabrication technology has been the main object of silicon photonics for decades. There have been a great number of studies for developing optical components integrated on silicon wafers including waveguides,

couplers, routers, hybrid lasers and modulators. Among those components, optical modulator is a key component for many interesting applications. Traditionally, optical modulators are made of materials with second order susceptibility tensor like lithium niobate, which rely on second-order nonlinear effect (Pockels effect). However, silicon is a centro-symmetric material that does not exhibit Pockels effect, therefore different modulation methods should be used. Largely two methods have been demonstrated for optical modulation in silicon. One is free carrier dispersion method that changing silicon's refractive index and absorption by modulating carrier concentration in active region. Devices of this category include carrier injection and carrier depletion. P-n junction configuration is usually used to achieve carrier injection or depletion by forward or reverse bias. This method is able to modulate as fast as several Gbit/s. However, optical loss increases as carrier concentration increases, therefore modulation depth is shallow. Another method is thermo optic modulation. Refractive index is modulated by temperature change of active area. Even though switching speed is slower than electro optic modulation, thermo optic modulation is more efficient in silicon due to its large thermo optic constant (dn/dT) and optical loss induced by temperature change is very small. Device designs are usually simpler and more compact compared to electro optic modulators. Therefore, thermo optic modulation in silicon can be a good alternative for applications that do not require fast switching speed. Efficient thermo-optic modulator materials require high thermo-optic constant (dn/dT) and low thermal conductivity. Also temperature dependent loss should be small. Silicon has high thermo-optic coefficient (150×10^{-4} K^{-1}), however high thermal conductivity is an obstacle for an efficient

modulator design. Previous study showed that porous silicon has reasonably high thermo-optic coefficient ($5\times\ 10^{-5}$ K^{-1} for 60% porosity) [60]. It has possibility to make efficient thermo-optic modulator coupled with its low thermal conductivity. It also eliminate complicated design and fabrication process of MOS SOI based silicon thermo-optic modulator. We are going to use our established waveguide fabrication and heater patterning techniques to build the device.

5.2.2 Non-contact method to investigate anisotropic thermal property

The 3-ω method usually works well for bulk materials or thin film with relatively low thermal conductivity compared to the substrate, and provides accurate results compared to more classical steady-state heating methods. However it requires rather large measurement sample (metal strip length is usually several millimeter), fabrication step for metal strip and reliable electrical contact between sample and the rest of experimental system. These are problematic constraints for modern microscale devices with small feature sizes and complicated structures. Micro devices including cantilevers, micro heaters, bolometers and actuators often use suspended thin films that are not readily amenable to patterning of large-area electrical contacts. Such devices require reliable characterization of the in-plane thermal conductivity. A solution to the above mentioned problems is to devise a measurement method that is able to sense the in-plane thermal conductivity directly without fabrication of additional heating and sensing structures, and without physical contact

between the sample and measurement system. A few non-contact thermal property measurement methods have been investigated, including micro-Raman, photoacoustic and thermoreflectance. However they are not capable of measuring in-plane component. Transient thermal grating (TTG) [61,62] is a promising optical-heating and optical-detection method that is able to measure in-plane thermal property directly. It uses interference fringes by two pump beam as a non-contact heating source and measure response of probe beam deflected by thermally induced grating on sample surface. In spite of its advantages including non-contact nature and direct in-plane measurement capability, TTG has not been widely investigated until today. The method has been used for measuring thermal conductivity of samples that have higher in-plane conductivity than cross-plane conductivity such as superlattice [56]. It would be useful if the TTG method can be adapted to characterize the thermal properties of above mentioned micro devices which comprise a number of different structures.

Bibliography

[1] L. T. Canham. Silicon quantum wire array fabrication by electrochemical and chemical dissolution of wafers. *Applied Physics Letters*, 57:1049, 1990.

[2] C. Mazzoleni and L. Pavesi. Application to optical components of dielectric porous silicon multilayers. *Applied Physics Letters*, 67:2983, 1995.

[3] Lorenzo Pavesi, Claudio Mazzoleni, Alessandro Tredicucci, and Vittorio Pellegrini. Controlled photon emission in porous silicon microcavities. *Applied Physics Letters*, 67:3280, 1995.

[4] Guoguang Rong, Judson D. Ryckman, Raymond L. Mernaugh, and Sharon M. Weiss. Label-free porous silicon membrane waveguide for DNA sensing. *Applied Physics Letters*, 93(16):2–4, 2008.

[5] Andrea M. Rossi, Lili Wang, Vytas Reipa, and Thomas E. Murphy. Porous silicon biosensor for detection of viruses. *Biosensors and Bioelectronics*, 23(5):741 – 745, 2007.

[6] Jun Gao, Ting Gao, Yang Yang Li, and Michael J. Sailor. Vapor sensors based on optical interferometry from oxidized microporous silicon films. *Langmuir*, 18(6):2229–2233, 2002.

[7] Luca De Stefano, Lucia Rotiroti, Ilaria Rea, Luigi Moretti, Girolamo Di Francia, Ettore Massera, Annalisa Lamberti, Paolo Arcari, Carmen Sanges, and Ivo Rendina. Porous silicon-based optical biochips. *Journal of Optics A: Pure and Applied Optics*, 8(7):S540–S544, July 2006.

[8] P. A. Snow, E. K. Squire, P. St. J. Russell, and L. T. Canham. Vapor sensing using the optical properties of porous silicon Bragg mirrors. *Journal of Applied Physics*, 86(4):1781, 1999.

[9] M. A. Anderson, A. Tinsley-Bown, P. Allcock, E. A. Perkins, P. Snow, M. Hollings, R. G. Smith, C. Reeves, D. J. Squirrell, S. Nicklin, and T. I.

Cox. Sensitivity of the optical properties of porous silicon layers to the refractive index of liquid in the pores. *Physica Status Solidi (a)*, 197(2):528–533, May 2003.

[10] S. Chan, P. M. Fauchet, Y. Li, L. J. Rothberg, and B. L. Miller. Porous silicon microcavities for biosensing applications. *Physica Status Solidi (a)*, 182(1):541–546, November 2000.

[11] Luca De Stefano, Ivo Rendina, Luigi Moretti, and Andrea Mario Rossi. Optical sensing of flammable substances using porous silicon microcavities. *Materials Science and Engineering: B*, 100(3):271–274, July 2003.

[12] Luca De Stefano, Luigi Moretti, Annalisa Lamberti, Olimpia Longo, Massimiliano Rocchia, Andrea M. Rossi, Paolo Arcari, and Ivo Rendina. Optical sensors for vapors , liquids , and biological molecules based on porous silicon technology. *IEEE Transactions on Nanotechnology*, 3(1):49–54, 2004.

[13] Lisa A. DeLouise, Peng Meng Kou, and Benjamin L. Miller. Cross-correlation of optical microcavity biosensor response with immobilized enzyme activity. Insights into biosensor sensitivity. *Analytical Chemistry*, 77(10):3222–30, May 2005.

[14] Hongyan Zhang, Zhenhong Jia, Xiaoyi Lv, Jun Zhou, Liangliang Chen, Rongxia Liu, and Ji Ma. Porous silicon optical microcavity biosensor on silicon-on-insulator wafer for sensitive DNA detection. *Biosensors & Bioelectronics*, 44C:89–94, January 2013.

[15] Rong Liu, Thomas A. Schmedake, Yang Yang Li, Michael J. Sailor, and Yeshaiahu Fainman. Novel porous silicon vapor sensor based on polarization interferometry. *Sensors and Actuators B: Chemical*, 87(1):58–62, November 2002.

[16] Jesús Alvarez, Paolo Bettotti, Isaac Suárez, Neeraj Kumar, Daniel Hill, Vladimir Chirvony, Lorenzo Pavesi, and Juan Martínez-Pastor. Birefringent porous silicon membranes for optical sensing. *Optics Express*, 19(27):26106–16, December 2011.

[17] Kyowon Kim and Thomas E. Murphy. Porous silicon integrated Mach-Zehnder interferometer waveguide for biological and chemical sensing. *Optics Express*, 21(17):19488–97, 2013.

[18] H. R. Shanks, P. D. Maycock, P. H. Sidlers, and G. C. Danielson. Thermal conductivity of silicon from 300 to 1400°K. *Physical Review*, 130(5):1743, 1963.

[19] C. J. Glassbrenner and Glen A. Slack. Thermal conductivity of silicon and germanium from 3°K to the melting point. *Physical Review*, 134(4A):1058, 1964.

[20] U. Bernini, P. Maddalena, E. Massera, and A. Ramaglia. Thermal characterization of porous silicon via thermal wave interferometry. *Optics Communications*, 168:305–314, 1999.

[21] U. Bernini, S. Lettieri, E. Massera, and P. A. Rucco. Investigation of thermal transport in n-type porous silicon by photo-acoustic technique. *Optics and Lasers in Engineering*, 39:127–140, 2003.

[22] S. Périchon, V. Lysenko, B. Remaki, D. Barbier, and B. Champagnon. Measurement of porous silicon thermal conductivity by micro-Raman scattering. *Journal of Applied Physics*, 86(8):4700–4702, 1999.

[23] V. Lysenko, S. Périchon, B. Remaki, D. Barbier, and B. Champagnon. Thermal conductivity of thick meso-porous silicon layers by micro-Raman scattering. *Journal of Applied Physics*, 86(12):6841, 1999.

[24] S. Périchon, V. Lysenko, Ph. Roussel, B. Remaki, B. Champagnon, D. Barbier, and P. Pinard. Technology and micro-Raman characterization of thick meso-porous silicon layers for thermal effect microsystems. *Sensors and Actuators*, 85:335339, 2000.

[25] S. Gomès, L. David, V. Lysenko, A. Descamps, T. Nychyporuk, and M. Raynaud. Application of scanning thermal microscopy for thermal conductivity measurements on meso-porous silicon thin films. *Journal of Physics D: Applied Physics*, 40(21):6677–6683, 2007.

[26] G. Gesele, J. Linsmeier, V. Drach, J. Fricke, and R. Arens-Fischer. Temperature-dependent thermal conductivity of porous silicon. *Journal of Physics D: Applied Physics*, 30:29112916, 1997.

[27] David G. Cahill. Thermal conductivity measurement from 30 to 750 k: the 3ω method. *Review of Scientific Instruments*, 61(2):802, 1990.

[28] Chris Dames and Gang Chen. 1ω,2ω, and 3ω methods for measurements of thermal properties. *Review of Scientific Instruments*, 76(12):124902, 2005.

[29] Chris Dames. Measuring the thermal conductivity of thin films: 3 omega and related electrothermal methods. *Annual Review of Heat Transfer*, 2013.

[30] H. Neff, J. Laukemper, I. A. Khrebtov, A. D. Tkachenko, E. Steinbeiss, W. Michalke, M. Burnus, T. Heidenblut, G. Hefle, and B. Schwierzi. Sensitive high-Tc transition edge bolometer on a micromachined silicon membrane. *Applied Physics Letters*, 66(18):2421, 1995.

[31] M. Kenyon, P. K. Day, C. M. Bradford, J. J. Bock, and H. G. Leduc. Background-limited membrane-isolated tes bolometers for far-ir/submillimeter direct-detection spectroscopy. *Nuclear Instruments and Methods in Physics Research Section A: Accelerators, Spectrometers, Detectors and Associated Equipment*, 559(2):456–458, 2006.

[32] Jesper B. Jensen, Lars H. Pedersen, Poul E. Hoiby, Lars B. Nielsen, T. P. Hansen, J. R. Folkenberg, J. Riishede, Danny Noordegraaf, Kristian Nielsen, A. Carlsen, and A. Bjarklev. Photonic crystal fiber based evanescent-wave sensor for detection of biomolecules in aqueous solutions. *Optics Letters*, 29(17):1974–6, September 2004.

[33] C. A. Rowe-Taitt, J. W. Hazzard, K. E. Hoffman, J. J. Cras, J. P. Golden, and F. S. Ligler. Simultaneous detection of six biohazardous agents using a planar waveguide array biosensor. *Biosensors & Bioelectronics*, 15(11-12):579–89, January 2000.

[34] Marie-Laure Anne, Julie Keirsse, Virginie Nazabal, Koji Hyodo, Satoru Inoue, Catherine Boussard-Pledel, Hervé Lhermite, Joël Charrier, Kiyoyuki Yanakata, Olivier Loreal, Jenny Le Person, Florent Colas, Chantal Compère, and Bruno Bureau. Chalcogenide glass optical waveguides for infrared biosensing. *Sensors*, 9(9):7398–411, January 2009.

[35] Pavel Polynkin, Alexander Polynkin, N. Peyghambarian, and Masud Mansuripur. Evanescent field-based optical fiber sensing device for measuring the refractive index of liquids in microfluidic channels. *Optics Letters*, 30(11):1273–5, June 2005.

[36] Stefania Campopiano, Romeo Bernini, Luigi Zeni, and Pasqualina M. Sarro. Microfluidic sensor based on integrated optical hollow waveguides. *Optics Letters*, 29(16):1894–6, August 2004.

[37] Víctor J. Cadarso, César Fernández-Sánchez, Andreu Llobera, Margarita Darder, and Carlos Domínguez. Optical biosensor based on hollow integrated waveguides. *Analytical Chemistry*, 80(9):3498–501, May 2008.

[38] Edoardo De Tommasi, Luca De Stefano, Ilaria Rea, Valentina Di Sarno, Lucia Rotiroti, Paolo Arcari, Annalisa Lamberti, Carmen Sanges, and Ivo Rendina. Porous silicon based resonant mirrors for biochemical sensing. *Sensors*, 8(10):6549–6556, October 2008.

[39] Ilaria Rea, Mario Iodice, Giuseppe Coppola, Ivo Rendina, Antigone Marino, and Luca De Stefano. A porous silicon-based Bragg grating waveguide sensor for chemical monitoring. *Sensors and Actuators B: Chemical*, 139(1):39–43, May 2009.

[40] Guoguang Rong. Highly sensitive porous silicon membrane waveguide sensor using ultra-high order mode. *2009 Symposium on Photonics and Optoelectronics*, pages 1–4, August 2009.

[41] Yang Jiao and Sharon M. Weiss. Design parameters and sensitivity analysis of polymer-cladded porous silicon waveguides for small molecule detection. *Biosensors & Bioelectronics*, 25(6):1535–8, February 2010.

[42] Xing Wei and Sharon M. Weiss. Guided mode biosensor based on grating coupled porous silicon waveguide. *Optics Express*, 19(12):11330–9, June 2011.

[43] A. Loni, L. T. Canham, M. G. Berger, R. Arens-Fischer, H. Munder, H. Luth, H. F. Arrand, and T. M. Benson. Porous silicon multilayer optical waveguides. *Thin Solid Films*, 276:143–146, 1996.

[44] J. Charrier, C. Lupi, L. Haji, and C. Boisrobert. Optical study of porous silicon buried waveguides fabricated from p-type silicon. *Materials Science in Semiconductor Processing*, 3(2000):357–361, 2000.

[45] P. Pirasteh, J. Charrier, Y. Dumeige, P. Joubert, S. Haesaert, and L. Haji. Further results on porous silicon optical waveguides at 1.55 μm. *Physica Status Solidi (a)*, 204(5):1346–1350, May 2007.

[46] M. Hiraoui, M. Guendouz, N. Lorrain, L. Haji, and M. Oueslati. Buried anti resonant reflecting optical waveguide based on porous silicon material for an integrated Mach Zehnder structure. *Applied Physics Letters*, 101(19):191114, 2012.

[47] Andrea M. Rossi, Giampiero Amato, Vittorio Camarchia, Luca Boarino, and Stefano Borini. High-quality porous-silicon buried waveguides. *Applied Physics Letters*, 78(20):3003–3005, 2001.

[48] Jinan Xia, Andrea M. Rossi, and Thomas E. Murphy. Laser-written nanoporous silicon ridge waveguide for highly sensitive optical sensors. *Optics Letters*, 37(2):256–8, January 2012.

[49] Xiang Zhang and Costas P. Grigoropoulos. Thermal conductivity and diffusivity of freestanding silicon nitride thin films. *Review of Scientific Instruments*, 66:1115, 1995.

[50] W. Lang, A. Drost, P. Steiner, and H. Sandmaier. The thermal conductivity of porous silicon. In *Symposium F Microcrystalline and Nanocrystalline Semiconductors*, volume 358 of *MRS Proceedings*, 1994.

[51] H. S. Carslaw and J. C. Jaeger. *Conduction of Heat in Solids*. Oxford Science Publications, 1947.

[52] C. Tsamis, A. G. Nassiopoulou, and A. Tserepi. Thermal properties of suspended porous silicon micro-hotplates for sensor applications. *Sensors and Actuators B: Chemical*, 95(1-3):78–82, 2003.

[53] R. Triantafyllopoulou, S. Chatzandroulis, C. Tsamis, and A. Tserepi. Alternative micro-hotplate design for low power sensor arrays. *Microelectronic Engineering*, 83(4-9):1189–1191, 2006.

[54] P. Ferrando-Villalba, A. F. Lopeandia, L. Abad, J. Llobet, M. Molina-Ruiz, G. Garcia, M. Gerbolès, F. X. Alvarez, A. R. Goñi, F. J. Muñoz Pascual, and J. Rodríguez-Viejo. In-plane thermal conductivity of sub-20 nm thick suspended mono-crystalline Si layers. *Nanotechnology*, 25(18):185402, 2014.

[55] W. Jang, Z. Chen, W. Bao, C. N. Lau, and C. Dames. Thickness-dependent thermal conductivity of encased graphene and ultrathin graphite. *Nano Letters*, 10(10):3909–3913, 2010.

[56] M. N. Luckyanova, J. A. Johnson, A. A. Maznev, J. Garg, A. Jandl, M. T. Bulsara, E. A. Fitzgerald, K. A. Nelson, and G. Chen. Anisotropy of the thermal conductivity in GaAs/AlAs superlattices. *Nano Letters*, 13(9):3973–7, 2013.

[57] T. Borca-Tasciuc, A. R. Kumar, and G. Chen. Data reduction in 3ω method for thin-film thermal conductivity determination. *Review of Scientific Instruments*, 72(4):2139, 2001.

[58] G. Chen, S.Q. Zhou, D. Y. Yao, C. J. Kim, X. Y. Zheng, Z. L. Liu, and K. L. Wang. Heat conduction in alloy-based superlattices. In *17th International Conference on Thermoelectrics. Proceedings*, pages 202–205, 1998.

[59] Jung Hun Kim, Albert Feldman, and Donald Novotny. Application of the three omega thermal conductivity measurement method to a film on a substrate of finite thickness. *Journal of Applied Physics*, 86(7):3959, 1999.

[60] Luigi Moretti, Luca De Stefano, Andrea M. Rossi, and Ivo Rendina. Dispersion of thermo-optic coefficient in porous silicon layers of different porosities. *Applied Physics Letters*, 86(6):061107, 2005.

[61] J. E. Graebner. Measurement of thermal diffusivity by optical excitation and infrared detection of a transient thermal grating. *Review of Scientific Instruments*, 66(7):3903, 1995.

[62] Jeremy A. Johnson, A. A. Maznev, John Cuffe, Jeffrey K. Eliason, Austin J. Minnich, Timothy Kehoe, Clivia M. Sotomayor Torres, Gang Chen, and Keith A. Nelson. Direct measurement of room-temperature nondiffusive thermal transport over micron distances in a silicon membrane. *Physical Review Letters*, 110(2), 2013.